Mass balance modelling and climate sensitivity of Saskatchewan Glacier, western Canada

Christophe Kinnard[1], Olivier Larouche[1], Michael N. Demuth[2], Brian Menounos[3]

[1] Département des Sciences de l'environnement, Université du Québec à Trois Rivières, Trois-Rivières, G87R7, Canada
[2] Geological Survey of Canada; currently, University of Saskatchewan Cold Water Laboratory, Canmore, T1W 3G1, Canada
[3] Natural Resources and Environmental Studies Institute and Geography, University of Northern British Columbia, Prince George, British Columbia, Canada

Correspondence to: Christophe Kinnard (christophe.kinnard@uqtr.ca)

Abstract. Glacier mass balance models are needed at sites with scarce long-term observations to reconstruct past glacier mass balance and assess its sensitivity to future climate change. In this study North American Regional Reanalysis (NARR) data are used to force a physically-based, distributed glacier mass balance model of Saskatchewan Glacier for the historical period 1979-2016 and assess it sensitivity to climate change. A two-year record (2014-2016) from an on-glacier automatic weather station (AWS) and a homogenized historical precipitation record from nearby permanent weather stations were used to downscale air temperature, relative humidity, wind speed, incoming solar radiation and precipitation from the nearest NARR gridpoint to the glacier AWS site. The model was run with fixed (1979, 2010) and time-varying (dynamic) geometry using a multi-temporal digital elevation model (DEM) dataset. The model showed a good performance against recent (2012-2016) direct glaciological mass balance observations as well as with cumulative geodetic mass balance estimates. The simulated mass balance showed a large sensitivity to the biases in NARR precipitation and solar radiation, as well as to the prescribed precipitation lapse rate and ice aerodynamic roughness lengths, showing the importance of constraining these parameters with ancillary data. The difference between the static (1979) and dynamic simulations showed small differences (mean = 0.06 m w.e. a^{-1} or 1.5 m w.e. over 37 yrs), indicating minor effects of elevation changes on the glacier specific mass balance. The static mass balance sensitivity to climate was assessed for prescribed changes in regional mean air temperature between 0 to 7 °C and precipitation between -20 to +20%, which comprise the spread of ensemble IPCC representative concentration pathways climate scenarios for the mid (2041-2070) and late (2071-2100) 21st century. The climate sensitivity experiments showed that future changes in precipitation would have a small impact on glacier mass-balance, while the temperature sensitivity increases with warming, from -0.65 to -0.93 m w.e. °C^{-1}. Increased melting accounted for 90% of the temperature sensitivity while precipitation phase feedbacks accounted for only 10%. Roughly half of the melt response to warming was driven by a positive albedo feedback, in which glacier albedo decreases as the snow cover on the glacier thins and recedes earlier in response to warming, increasing net solar radiation fluxes. About one quarter of the melt response to warming was driven by latent heat energy gains (positive humidity feedback). Our study underlines the key role of albedo and air humidity in modulating the response of winter-accumulation type mountain glaciers and upland icefield-outlet glacier settings to climate.

1 Introduction

Global warming is expected to cause reduced snowfall in cold regions, earlier snowmelt in spring and a longer ice melt period in summer (e.g. Aygün et al., 2019; Barnett et al., 2005). Even if the amount of precipitation remains unchanged, warming

35 alone will reduce snow and ice storage in catchments, affecting the seasonality of river streamflow regimes and accelerating water losses to the ocean (Barnett et al., 2005; Escanilla-Minchel et al., 2020; Huss et al., 2017; Huss and Hock, 2018). Glaciers act as natural reservoirs in mountain regions, contributing fresh water during periods of drought and buffering the hydrological regimes of rivers against extreme climate variability (Fountain and Tangborn, 1985; Jansson et al., 2003). The transition from a nivo-glacial to a more pluvial river regime in response to warming would change the timing and magnitude of floods, leading

40 to altered patterns of erosion and sediment deposition and impacting biodiversity and water quality downstream (Déry et al., 2009; Huss et al., 2017). The impacts of the progressive loss of ice and snow surfaces and resulting alterations of the hydrological cycle can reach well beyond the glacierized catchments, affecting agriculture (Barnett et al., 2005; Comeau et al., 2009; Milner et al., 2017; Schindler and Donahue, 2006), fisheries (Dittmer, 2013; Grah and Beaulieu, 2013; Huss et al., 2017), hydropower and general ecological integrity (Huss et al., 2017). Glaciers and ice caps (GIC) mass loss have also contributed

45 to sea level rise over the last decades, with recent estimates of 0.48 ± 0.1 mm a^{-1} between 1992 and 2016 for GIC excluding Greenland and Antarctica peripheral ice caps and glaciers (PGIC) (Bamber et al., 2018), and 0.5 ± 0.4 mm a^{-1} (with PGIC) or 0.4 ± 0.3 mm a^{-1} (without PGIC) between 1961 and 2016 (Zemp et al., 2019). Mass loss from GIC could increase sea-level by 0.215 ± 0.021 m at the end of the 21st century under high-end climate change scenarios (Shannon et al., 2019), exacerbating coastal inundations and forcing population movement in several areas of the world (Cazenave and Cozannet, 2014).

50

The surface mass balance is the prime variable of interest to monitor and project the state of glaciers and their hydrological contribution under global warming scenarios. Only few glaciers around the world have long term direct mass balance observations because these measurements are time consuming and logistically complicated. Geodetic estimates provide a complementary picture of cumulative mass changes for a greater number of glaciers worldwide, but their coarser sampling

55 interval (typically > 5years) makes their link with climate less direct (Cogley, 2009; Cogley and Adams, 1998; Menounos et al., 2019). For this reason, models are often used to extrapolate scarce measurements, estimate unsampled glaciers and to assess glacier mass balance sensitivity to climate. Several types of mass balance models have been used, whose complexity varies depending on the processes represented, the input data required and the spatial and temporal resolution of the models. The so-called 'temperature-index' or 'degree-days' models use only air temperature as sole predictor of ablation (Hock, 2003).

60 These models have been extensively used to project regional and global glacier mass balance under climate change scenarios, due to their simple implementation and readily available global precipitation and temperature forcing data (Hock et al., 2019; Huss and Hock, 2015; Marzeion et al., 2012; Radić et al., 2014). Enhanced temperature-index models include additional predictors such as potential (Hock, 1999) or net (Pellicciotti et al., 2005) solar radiation to estimate melt. They offer a useful

trade-off between the simple temperature-index models and the more complex energy-balance models and have been shown to be more transferable outside their calibration interval (Gabbi et al., 2014; Réveillet et al., 2017). Simple empirical models contain few parameters that simplifies their application, but they must be calibrated with observations. The extrapolation of parameters in time and space, i.e., outside their calibration conditions, is therefore questionable (Carenzo et al., 2009; Gabbi et al., 2014; Hock et al., 2007; Wheler, 2009). Alternatively, spatially-distributed, physically-based models rely on energy balance calculations to explicitly account for all energy exchanges between the glacier surface and atmosphere. They are more complex and contain several parameters that are sometimes difficult to estimate and require several input observations (e.g. Anderson et al., 2010; Anslow et al., 2008; Arnold et al., 1996; Gerbaux et al., 2005; Hock and Holmgren, 2005; Klok and Oerlemans, 2002; Mölg et al., 2008). However, these models better represent the physical processes which drive glacier ablation and are thus more suited to simulate glacier mass balance outside of present-day climate conditions (Hock et al., 2007; MacDougall and Flowers, 2011), given that accurate forcing data is available (Réveillet et al., 2018). This makes physically-based distributed models an ideal tool to estimate glacier climate sensitivity, i.e., the mass balance response to a change in climate conditions (Braithwaite and Raper, 2002; Che et al., 2019; Ebrahimi and Marshall, 2016; Engelhardt et al., 2015; Hock et al., 2007; Klok and Oerlemans, 2004; Oerlemans et al., 1998).

Glaciological models have been mostly forced with observations from automatic meteorological stations (AWS) on or near glaciers. However, the management of weather stations networks in mountainous areas poses financial and logistical challenges. At sites with scarce or missing data, outputs from meteorological forecasting models (Bonekamp et al., 2019; Mölg et al., 2012; Radic et al., 2018) and downscaled reanalysis data (Clarke et al., 2015; Hofer et al., 2010; Østby et al., 2017; Radić and Hock, 2006) have been used to force physically-based model. Reanalyses are produced by retrospective numerical weather model simulations that assimilate long-term and quality-controlled observations and provide consistent gridded estimates of past atmospheric states at sub-daily intervals. They offer useful alternatives to drive glaciological and hydrological models in data-scarce regions (Hofer et al., 2010). However, reanalysis data are typically produced at longer time intervals and coarser spatial resolutions than observations, e.g. from 4-times daily and ~210 km for NCEP/NCAR Reanalyses (Kistler et al., 2001), to hourly and ~30 km for the recent ERA-5 product (Hersbach and Dee, 2016). Regional products like the North American Regional Reanalysis (NARR) were developed to enhance the spatial and temporal resolution of reanalyses at the continental scale (Mesinger et al., 2006). Statistical downscaling of reanalysis data using on- or near-glacier meteorological observations has been used in order to reduce biases resulting from this temporal and spatial scale mismatch as well as from structural and parameterizations errors in the reanalysis model (Hofer et al., 2010). Several methods can be used to correct those errors, such as a simple bias shift toward observations (scaling or delta method) or the matching of two probability distributions (e.g. quantile mapping) (Radić and Hock, 2006; Rye et al., 2010). This step is crucial, as uncertainties in climate forcing can be the main source of error in mass balance modelling (Østby et al., 2017).

The Canadian Rocky Mountains support many glaciers which provide several ecosystem services, such as water provision for hydropower production and agriculture, and constitute iconic features highly valorized for tourism (Anderson and Radić, 2020; Comeau et al., 2009; Moore et al., 2009; Petts et al., 2006; Schindler and Donahue, 2006). Bolch et al. (2010) compared

100   satellite images from 1985 to 2005 and reported an 11% (± 3.8%) loss of glacier area in western Canada. A later study reported a 30% decrease in glacier surface area, representing 750 km² in the central and southern Canadian Rockies over the period 1919-2006 (Tennant et al., 2012), while Demuth et al. (2008) determined glacier area-wise losses of 22% and 36% in the North and South Saskatchewan River Basins respectively between 1978 and 1998. Only a few glaciers have been directly and continuously monitored for mass balance in the Canadian Rockies. Peyto Glacier (51.67 °N, -116.53 °E) is the only reference

105   site with a long mass balance record (since 1966), and with the exception of 1996 and 2000, exhibits a consistent trend of negative annual balance beginning since the mid-1970's (Demuth, 2018; Demuth et al., 2006; Demuth and Pietroniro, 2002). No other long-term records exist to assess mass balance variations and trends in the region. Menounos et al. (2019) recently used multisensor digital elevation models from spaceborne optical imagery to calculate a mean mass balance of 0.410 ± 0.213 m w.e. a^{-1} for the 2000-2018 period in the Canadian Rocky Mountains, with accelerated mass loss between 2000-2009 and

110   2009-2018. A recent large-scale modelling study showed that the volume of western Canada's glaciers could decrease by 70% (± 10%) from 2005 to 2100, and could exceed 90% in the Rockies region (Clarke et al., 2015). Clarke et al. (2015) concluded that the main source of uncertainty in their simulations of glacier evolution at the mountain range scale was not the parameterisation of glacier flow but rather the simulation of surface mass balance. Thus, accurate models of surface mass balance are still needed at the scale of individual glaciers, to extend, and give context to, sparse mass balance observations as

115   well as to characterize the mass balance sensitivity to climate change. Saskatchewan Glacier, one of the main outlet glaciers of the Columbia Icefield in the Canadian Rocky Mountains (52.15 °N, -117.29 °E), is such a glacier with sparse mass balance observations available only since 2012, which challenges the application of physically-based mass balance models.

This study uses a physically-based, distributed mass balance model in the context of sparse observations to reconstruct long-

120   term glacier mass changes and spatiotemporal patterns of energy and mass fluxes, and to investigate the glacier mass balance sensitivity to climate change. While the climate sensitivity of mass-balance has been investigated in several previous studies, the present study addresses the comparatively unexplored topics of the respective contributions of ablation versus precipitation phase feedbacks to the temperature sensitivity of glaciers, and of the changing contribution of energy fluxes driving the changes in glacier melt under warming scenarios.

125   **2 Study area**

The Columbia Icefield is located in the Canadian Rocky Mountains and straddles the border between Alberta and British Columbia (Figure 1a). The Columbia Icefield is accessible via the Icefields Parkway which is surrounded by two national parks (Jasper, and Banff), which makes the Columbia Icefield a highly-valued cultural and touristic site (Sandford, 2016).
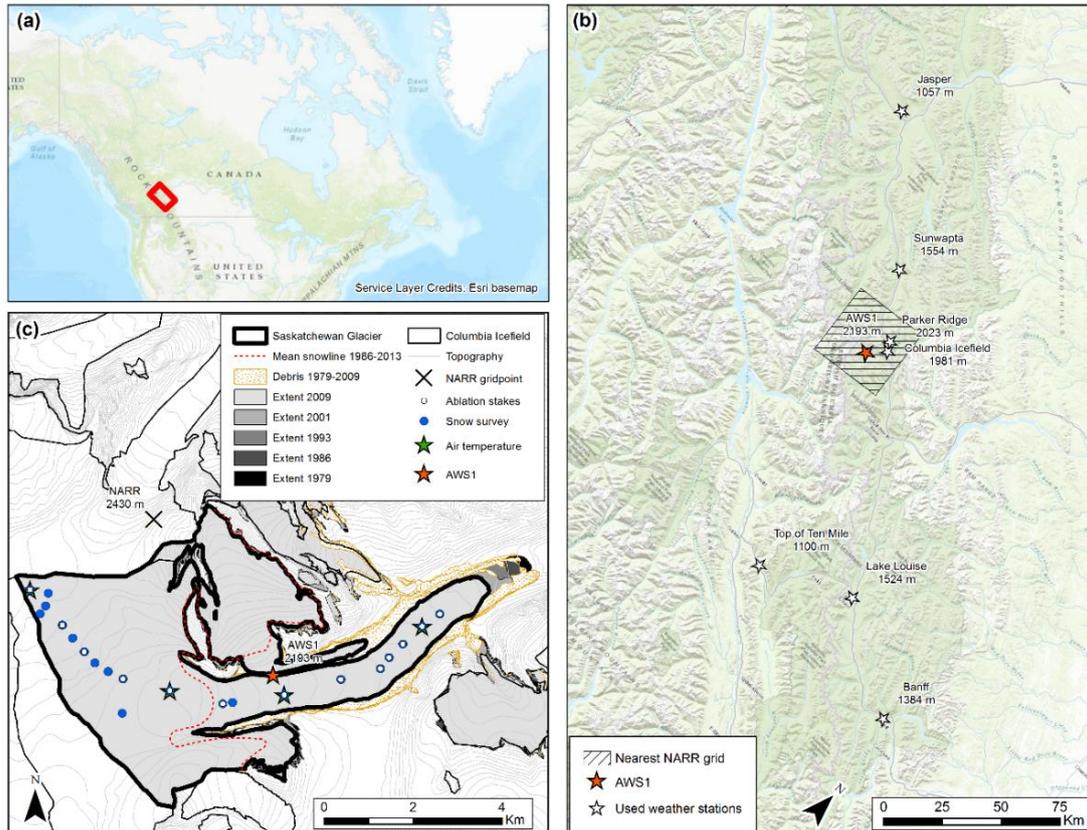
Figure 1. Study area map. (a) Location of the Columbia Icefield in the Canadian Rockies; the red rectangle shows the area of panel b. (b) Weather stations from the permanent network used to calculate temperature and precipitation lapse rate. The nearest NARR gridpoint (hatched square) is located directly above neighbouring Athabasca Glacier and encompasses Saskatchewan Glacier. (c) Map of Saskatchewan Glacier showing the location of ablation stakes and additional snow survey points, and air temperature sensors used to determine the diurnal lapse rate over the glacier. The mean end of summer snow line position (1986-2013) is shown by a red dotted line.

The plateau lying at ~2800 meters above sea level (m a.s.l) intercepts moist air masses originating from the Pacific Ocean, which results in large snow accumulation and the formation of glacial ice flowing downward through several outlet glaciers (Demuth and Horne, 2018). The Columbia Icefield is of crucial importance to the region's water budget, as it feeds three different continent-scale watersheds flowing towards the Arctic, Pacific and Atlantic oceans (Figure 1a). The main and largest outlet glaciers are located east of the icefield (Saskatchewan and Athabasca Glacier), draining ~60% of the eastern Columbia Icefield to the North Saskatchewan River (Hudson/Atlantic) and the Sunwapta-Athabasca River (Arctic) (Marshall et al., 2011). Tennant and Menounos (2013) used historical aerial photographs and satellite images to reconstruct the extent and volume changes of the Columbia Icefield. The area of the Columbia Icefield was estimated to be 265.1 ± 12.3 km² in 1919. By 2009 the icefield had declined by 59.6 ± 1.2 km² in 2009 at a rate of -0.66 ± 0.01 km² a⁻¹. Saskatchewan Glacier is the

largest outlet glacier of the icefield, presently covering an area of roughly 23 km² and ranging in elevation from 1784 to 3322 m, the summit of Mount Snow Dome - the hydrological apex of western Canada (Ednie et al., 2017). Saskatchewan Glacier experienced the greatest absolute area loss among the icefield glaciers, at 10.1 ± 0.6 km² a^{-1} since 1919 (Tennant and Menounos, 2013).

3 Data and Methods

3.1 Topographic data

The main topographic data used in this study is a 1-meter resolution digital elevation model (DEM) derived from two WorldView-2 (WV2) satellite stereo images acquired on July 31, 2010, covering the lower glacier and September 18, 2010, covering the upper glacier. The DEM was mosaiced with tiles from the Canadian Digital Surface Model (CDSM) (20-meter resolution) to include all topography adjacent to the glacier that could cast shadows on the glacier. The merged DEM was resampled to 100 meters resolution to allow faster calculation with the mass balance model. The firn area was delimited by a mean snowline delineated from Landsat satellite images from year 1986 to 2013 (Figure 1c). Eighteen cloud-free images were chosen near the end of the hydrological season (September 30) and used to map the mean transient snowline position at the end of summer, which was used as a proxy for the equilibrium line altitude (ELA). Image dates ranged between August 22 and October 2, necessary to find cloud-free images capturing the transient snow line near the end of the ablation period. To take into account historical glacier contraction in mass balance simulations, multi-temporal DEMs and glacier boundaries from Tennant and Menounos (2013) (hereafter 'TM2013') were used to update the glacier geometry over time in the mass balance model. TM2013 derived DEMs and glacier extents from aerial stereo photographs from 1979, 1986 and 1993. For 1999, they used the Shuttle Radar Topography Mission (SRTM) DEM of February 2000, which they attributed to best represent the glacier surface at the end of the 1999 summer ablation season, due to the penetration of the radar wave in the following year's winter snowpack. The glacier extent in 1999 was derived from the closest cloud-free, 30 m resolution Landsat 5 Thematic Mapper (TM) image in September 2001. The 2009 DEM and glacier extent from TM2013 were derived from Satellite Pour l'Observation de la Terre 5 (SPOT 5) stereo images with a resolution of 2.5 m. Points matched on stereoscopic image pairs were gridded to a 100 m resolution in the ablation area and to 200 m in the accumulation area where low contrasts resulted in a smaller number of elevation points, and varying amounts of data gaps. We re-interpolated all TM2013 DEMs to continuous 100 m resolution using shape-preserving linear interpolation. The 2010 WV2 DEM was used instead of the 2009 DEM from TM2013, which particularly suffered from extensive gaps in the accumulation zone, but the glacier extent of August 2009 was conserved as boundary for the 2010 WV2 DEM. The slope, aspect and sky-view factors were derived from all DEMs to be used as inputs for the mass balance model. Two static mass balance simulations were performed, one using the 1979 DEM as initial boundary condition, and the other with the 2010 DEMs. These were compared with a dynamical simulation in which the glacier geometry was adjusted with the multitemporal DEMs, to consider the impact of glacier recession on mass balance.

The TM2013 glacier boundaries were used but two ice masses, disconnected from Saskatchewan Glacier since 1979, were excluded from the original TM2013 outlines (see Figure 1c). The lateral, debris-covered moraines were also excluded from the glacier outlines. A more recent, 2-m resolution DEM was built from a stereo pair of Pleiades Satellite panchromatic images
180   acquired in September 2016 and using the NASA Ames Stereo Pipeline (ASP) (Shean et al., 2016). This DEM was used to update the geodetic mass balance from TM2013 (Supplementary Material). Since the 2010 WV2 DEM has the highest resolution and few gaps, it was considered the most reliable and used for model calibration and climate sensitivity experiments.

3.2 Meteorological data

3.2.1 On-glacier automatic weather station

185   An automatic weather station (AWS) was deployed in August 2014 on the medial moraine of Saskatchewan Glacier at an altitude of 2193 m a.s.l., collecting near-continuous hourly data for a two-year period, until June 2016 (Figure 1c). Recorded variables include air temperature (Ta), relative humidity (RH), incoming global (G) and reflected (SWout) solar radiation, and wind speed (WS) and direction (WD). *HOBO*[TM] air temperature sensors were installed by the GSC on five ablation stakes (Figure 1c) between May to August 2015, shielded from solar radiation using naturally ventilated gill shields. The data were
190   used to calculate a mean diurnal cycle for the air temperature lapse rate on the glacier, diurnal lapse rate variations having been shown to affect glacier melt simulations (Petersen and Pellicciotti, 2011). The mean diurnal glacier lapse rate cycle was combined with a mean monthly lapse rate estimated from the permanent weather station network (c.f. Sect. 3.2.2).

3.2.2 Meteorological data from permanent weather monitoring network

Mean monthly air temperature lapse rates and a constant precipitation lapse rate were calculated from the permanent weather
195   monitoring network maintained by Environment and Climate Change Canada. Seven weather stations with available air temperature data during the study period were chosen, ranging in elevation from 1050 to 2025 m a.s.l. (Figure 1b). A mean monthly lapse rate was calculated by linear regression of mean temperature against elevation, using a minimum of 5 stations for each month depending on available data. Mean diurnal anomalies in the glacier lapse rate, described in the previous section, were added to the monthly lapse rates. As precipitation was not measured at the AWS site, a homogenized historical
200   precipitation record was produced using data from the two weather stations closest to Saskatchewan Glacier (Parker Ridge, 2023 m a.s.l. and Columbia Icefield, 1981 m a.s.l., see Figure 1b). The Columbia Icefield station was only operated between May and November while Parker Ridge was operated mostly in winter and sometimes all year-round depending on road accessibility. Both discontinuous records were combined into a single homogenised record. Because data gaps remained, reanalysis data corrected with the homogenised precipitation record was used instead to force the mass balance model (c.f.
205   Sect. 3.2.3). As the glacier mass balance model only considers a constant precipitation lapse rate, a mean lapse rate of 15.6% 100 m^{-1} was calculated from the weather station network for the months of November to March, when snow precipitation is

most abundant on the glacier and the relation between precipitation and elevation is strongest (Supplementary Material). The standard deviation ($\pm 4\%$ 100 m^{-1}) was used to examine the sensitivity of modelled mass balance to the precipitation lapse rate.

3.2.3 Reanalysis data

210 While the precision of the on-glacier AWS data is useful to characterize the glacier microclimate, its short and discontinuous record is not adequate to drive a physically-based, distributed glacier mass balance model for periods of a decade or more. Meteorological reanalysis data were thus used to force the mass balance model over the period 1979-2016, and the AWS data was used to apply a first-order bias correction to the reanalysis data. Data from the North American Regional Reanalysis (NARR) (Mesinger et al., 2006) were chosen for this study because of its higher temporal (3 h) and spatial (32 km) resolution

215 compared to other commonly used products, such as ERA interim and NCEP reanalyses. The newer and higher resolution ERA5 reanalyses were not available at the time of analysis; moreover ERA5 reanalyses may also overpredict snowfall (Orsolini et al., 2019). NARR precipitation have been found to be superior to other global reanalysis products (Bukovsky and Karoly, 2007) and to represent well air temperature and humidity at high altitude sites in southern BC, Canada (Trubilowicz et al., 2016). NARR data for the gridpoint closest to Saskatchewan Glacier (see Figure 1) were acquired from the National Center

220 for Environmental Prediction (NCEP) at the National Centers for Atmospheric Research (NCAR). The NARR gridpoint elevation is 2430 m a.s.l., i.e. 237 m higher than the elevation of the glacier AWS used to downscale the data. The following variables were used: (i) instantaneous values of air temperature and relative humidity at 2 m above the surface (TMP2m-ANL, RH2m-ANL), (ii) wind speed vectors at 10 m above the model surface (U and V wind components: UGRD10m-ANL, VGRD10m-ANL), (iii) surface 3-hourly accumulated precipitation (APCPsfc-ACC), (iv) 3-hourly averaged surface downward

225 shortwave radiation fluxes (DSWRFsfc-AVE) and (v) instantaneous values of total cloud cover (CC: TCDClm-3hr). The 3-hourly data were interpolated to an hourly interval using linear interpolation and compared with the glacier AWS observations from 2014-2016. 3-hourly NARR variables were interpolated to the center of the hourly averaging interval used by the AWS datalogger. For instantaneous variables (ANL) the concurrent time tag was used for the interpolation while for averages (AVE) the time at the center of the averaging interval was used. The 3-hourly accumulated (ACC) precipitation totals were

230 disaggregated to hourly values by dividing the 3-hour totals into three exact quantities. Both incoming solar radiation and air temperature have strong diurnal cycles at the AWS site. Over the year, solar noon varies between 12 h 41 to 12 h 56 and sunshine duration varies between 7.75 to 16.75 hours. The 3-hourly NARR data could thus underestimate the daily peaks in solar radiation and air temperature, especially since the midday NARR 3 hourly average value spreads between 11 h 00 and 14 h 00. Given that solar noon occurs near the middle of this interval, however, the NARR midday solar radiation average may

235 in fact well approximate the peak mid-day value, while the 14 h 00 instantaneous temperature value is close to the time of maximum daily temperature. Nevertheless, to reduce the probability of the diurnal cycle being attenuated in the interpolated NARR data, a shape-preserving piecewise cubic interpolation was used to interpolate these variables to an hourly interval.

The NARR meteorological variables (Ta, RH, WS, G) were downscaled to the AWS site using a simple bias correction procedure using the MeteoLab (ML) Matlab® Toolbox (Cofiño et al., 2004). Because precipitation was not measured at the glacier AWS, the homogenized historical precipitation record was used to downscale the NARR precipitation data. Two simple bias correction methods: i) scaling and ii) empirical quantile mapping (EQM) (e.g. Teutschbein and Seibert, 2012; Wetterhall et al., 2012), were applied and compared. The scaling method is the simplest, in which the NARR outputs are scaled with the difference (additive correction) or quotient (multiplicative correction) between the mean NARR and mean observations. An additive correction is used for unbounded variables (Ta) and a multiplicative correction for strictly positive variables (RG, WS, G and P) as it also preserves the frequency. Because errors in incoming solar radiation can originate from improper representation of the atmospheric transmissivity and cloud cover in NARR or shading differences between the NARR smoothed topography and the real topography surrounding the AWS, a time-varying scaling method was used to correct the NARR global shortwave radiation data (G). A mean diurnal multiplicative correction factor was calculated by scaling the mean observed diurnal G cycle with that of the hourly-interpolated NARR. A separate diurnal correction factor was calculated for each month of the year, to account for the seasonality in sun angle and related errors between NARR and observations. The bias correction methods were evaluated against the glacier AWS data using split sample cross-validation, and compared with the baseline performance, i.e., without corrections to the NARR variables. The AWS data was split into two one-year sub-periods on which downscaling methods were respectively calibrated and validated; then both sub-periods were inverted, and the mean validation statistics calculated. For precipitation the entire historical record was used, so validation sub-periods are longer than for other variables. The Pearson correlation coefficient (R), mean error (bias), root mean square error (RMSE) and mean absolute error (MAE) were used for performance assessment. The downscale performance was evaluated at both hourly and daily time intervals.

3.3 Mass balance model

The physically-based, distributed glacier mass balance model DEBAM (Hock and Holmgren, 2005) was used to simulate the mass balance of Saskatchewan Glacier over the period 1979-2016. The surface mass balance is expressed as:

$$b(t) = Ps(t) - M(t) - S(t) \tag{1}$$

Where $b(t)$ is mass balance at time t, Ps is snow precipitation, M is melt and S is sublimation. Total precipitation is extrapolated to the model grid from the altitude of the homogenized reference station (2000 m a.s.l.) using the constant gradient calibrated from weather stations (c.f. Sect. 3.2.2). Total precipitation is split between rain and snowfall according to a threshold temperature ($T0$) of 1.5 °C, at which 50% of the precipitation falls as snow and 50% as rain. This value corresponds to a typical rain-snow temperature threshold for continental mountain ranges and was inferred from the relative humidity at the AWS site (83%) following Jennings et al. (2018). A linear interpolation of the rain/snow fraction is performed between $T0$-1 °C (100% snow) and $T0$+1 °C (100% rain).

270 The model calculates the distributed mass and energy balance on each grid cell from hourly meteorological forcing data including air temperature, relative humidity, precipitation, wind speed and incoming shortwave radiation (SWin). The energy at the surface available for melt on the glacier, Q_M (W m^{-2}), was calculated according to Eq. (2) and converted into meltwater equivalent M (mm h^{-1}) using the latent heat of fusion:

$$Q_M + Q_G + Q_R + Q_L + Q_H + L\uparrow + L_S\downarrow + L_T\downarrow + (1-\alpha)(I + D_S + D_T) = 0 \qquad (2)$$

275 where I is the direct (beam) incoming shortwave solar radiation, D_S and D_T are the diffuse sky and terrain shortwave radiation, respectively, α is the albedo, $L_S\downarrow$ and $L_T\downarrow$ are the longwave sky and terrain irradiance, respectively, $L\uparrow$ is longwave outgoing radiation, Q_H is the sensible-heat flux, Q_E is the latent-heat flux and Q_R is the energy supplied by rain (Hock and Holmgren, 2005). The ground heat flux in the ice or snow, Q_G, is often small for temperate glaciers and was neglected. Fluxes are positive towards the glacier surface and measured or calculated in W m^{-2}. The model allows for different parameterizations for

280 calculating energy balance components, depending on the availability of forcing data and calculation speed. The parameterizations used in this work are detailed in the next subsections.

3.3.1 Shortwave incoming radiation

The global solar radiation (G) from NARR downscaled at the AWS location is separated into the direct (I) and diffuse (D) components, which are then extrapolated individually to each gridcell considering terrain effects of the multitemporal DEMs.

285 Following Hock and Holmgren (2005), the separation is based on an empirical relationship between the ratio of measured global radiation to top-of-atmosphere radiation, G/I_{TOA}, and the ratio of diffuse to global radiation, D/G. Total diffuse radiation D calculated at the AWS is then subtracted from the global radiation to yield the direct solar radiation at the AWS site, I_S. Topographic shading is calculated at each hour and for each gridcell from the path of the sun and the effective horizon. If the AWS is shaded by surrounding topography, any measured global radiation is assumed diffuse. Direct radiation I is obtained

290 at each gridcell following Hock and Holmgren (2005) as:

$$I = \frac{I_S}{I_{SC}} I_C \qquad (3)$$

where the subscript s refers to the location of the climate station and c denotes clear-sky conditions. I_C is the potential clear-sky direct solar radiation which accounts for the effects of slope and aspect of each grid cell, as well as shading from surrounding topography. The ratio I_S/I_{SC} measured at the AWS accounts for deviations from clear-sky conditions, expressing

295 the reduction of potential clear-sky direct solar radiation mainly due to clouds, and is assumed to be spatially constant. Eq. (3) can not be applied when the AWS is shaded, since $I_C = 0$. In this case and for glacier grid cells that remain illuminated, the last ratio that could be obtained before the AWS grid cell become shaded is applied, which assumes that cloud conditions remain constant until the climate station is illuminated again (usually the next morning). The impact of this assumption on the

radiative balance is considered to be small because this situation occurs at low sun illumination angles. The total diffuse
300 radiation (D) is calculated as:

$$D = D_0 F + \alpha_m G(1 - F) \qquad (4)$$

where the first righthand term represents sky radiation (D_S) and the second term terrain radiation (D_T). D_0 is diffuse radiation
from an unobstructed sky calculated at the AWS and is considered spatially constant. F is the grid cell sky-view factor defined
by Oke (1987) and G is the downscaled NAAR global radiation at the AWS. The mean albedo (α_m) of the surrounding terrain
305 obtained for every hour is the arithmetic mean of the modelled albedo of all grid cells for the entire glacier (Hock and
Holmgren, 2005).

3.3.2 Albedo

The albedo parameterisation of Oerlemans and Knap (1998) was used to simulate the albedo (α):

$$\alpha_{snow}(t) = \alpha_{firn} + \left(\alpha_{frsnow} - \alpha_{firn}\right) exp \left(\frac{s-t}{t^*}\right) \qquad (5)$$

310 $$\alpha(t) = \alpha_{snow}(t) + \alpha_{ice} - \alpha_{snow}(t) \, exp \left(\frac{d}{d^*}\right) \qquad (6)$$

where $\alpha_{snow}(t)$ is snow albedo, $\alpha(t)$ the final glacier albedo at time t, α_{firn} is the characteristic albedo of firn, α_{frsnow} is the
characteristic albedo of fresh snow and α_{ice} is the characteristic albedo of ice. The time scale (t^*) determines how fast the
snow albedo decays over time (days) and approaches the firn albedo after a fresh snowfall, d^* is a characteristic snow depth
scale (cm) controlling the transition from snow albedo to ice albedo, s is the day of the last snowfall and d is snow depth (cm).
315 The constant, characteristic albedo values were set to $\alpha_{frsnow} = 0.9$ for fresh snow based on observations at the AWS. Ice
albedo was mapped using 17 of the 18 cloud-free, end-of-summer Landsat images used to delineate the mean snowline
position. Atmospherically corrected surface reflectance from the Landsat 5 ETM and Landsat 7 ETM+ sensors were converted
to broadband albedo following Knap et al. (1999). A median albedo map was produced, from which the distribution of ice
albedo values was extracted in a region of interest extending below the mean snowline and excluding the glacier margins
320 where shade effects were noticed (Supplementary Material). The median of the distribution (0.24) was used as the
representative ice albedo (α_{ice}) and the standard deviation (0.03) used as uncertainty range for sensitivity analysis. The
characteristic time (t^*) and depth (d^*) scales were calibrated using snow depth and albedo measurements at the AWS. Since
the AWS was on a moraine the value for α_{ice} was set instead to the measured soil albedo for calibration purposes. The optimum
values of $t^* = 14$ day and $d^* = 3$ cm were used in the model.

3.3.3 Atmospheric incoming longwave calculation

The atmospheric incoming longwave radiation (LWin) is calculated based on the parameterisation of Konzelmann et al. (1994),
which relies on independent variables of air temperature, vapour pressure and cloud cover according to Eq. (7):

$$LWin = [\varepsilon_{cs}(1 - n^p) + \varepsilon_{oc}n^p]\sigma Ta^4 \tag{7a}$$

$$\varepsilon_{cs} = 0.23 + 0.443\left(\frac{e}{Ta}\right)^{1/8} \tag{7b}$$

330 where ε_{cs} is the clear-sky emissivity, n is the fractional cloud cover fraction (0-1) derived from NARR cloud cover, σ is the Stefan-Boltzmann constant (5.67×10^8 m^{-2} K^{-4}) and Ta is the downscaled NARR air temperature in Kelvin. The overcast sky emissivity ($\varepsilon_{oc} = 0.968$) and exponent $p = 2$, were left to default values in DEBAM. We adjusted the emissivity calculation in DEBAM to include the spatial variability in air temperature since the default parameterisation only used Ta measured at the AWS location for the entire glacier area. This led to an overestimation of melt in the accumulation zone and an underestimation 335 in the ablation zone – both corrected when including the distributed Ta in Eq. 7a.

3.3.4 Turbulent heat fluxes

The turbulent sensible (Q_H) and latent (Q_E) heat fluxes were calculated from the bulk aerodynamic method (Hock and Holmgren, 2005) based on air temperature (Ta), wind speed (WS) and vapour pressure (e_z) at height (z) above the surface:

$$Q_H = \rho C_p \frac{k^2}{\left[ln\left(\frac{z}{z_{0w}}\right) - \psi_M\left(\frac{z}{L}\right)\right]\left[ln\left(\frac{z}{z_{0T}}\right) - \psi_M\left(\frac{z}{L}\right)\right]} WS_z(Ta_z - T_0) \tag{8}$$

340 $$Q_E = L_v \frac{0.623\rho_0}{P_0} \frac{k^2}{\left[ln\left(\frac{z}{z_{0w}}\right) - \psi_M\left(\frac{z}{L}\right)\right]\left[ln\left(\frac{z}{z_{0e}}\right) - \psi_M\left(\frac{z}{L}\right)\right]} WS_z(e_z - e_0) \tag{9}$$

where ρ is air density at sea level (1.29 kg m^{-3}), P_0 is the mean atmospheric pressure at sea level (101325 Pa), C_p is the specific heat capacity of air (1005 J kg^{-1} K^{-1}), k is the von Kármán's constant (0.4), T_0 is the surface temperature in Kelvin, e_0 is the surface vapour pressure in Pa, z_{0w}, z_{0T} and z_{0e} are the roughness lengths for the logarithmic profiles of wind speed, temperature and water vapour, respectively, ψ_M, ψ_H and ψ_E are the stability functions, L is the Monin–Obukhov length, and 345 L_v is the latent heat of evaporation (2.514×10^6 J kg^{-1}) or sublimation (2.849×10^6 J kg^{-1}), depending on surface temperature and the direction of the latent heat flux. If Q_E is positive, condensation occurs if the surface is melting, or deposition if the surface is frozen. Sublimation occurs when Q_E is negative. The aerodynamic roughness length (z_0) for snow and ice influences the intensity of turbulent fluxes at the glacier surface. Typical z_0 values for glacier snow (z_{0_snow}) range between 0.5 and 6 mm (Brock et al., 2006; Fitzpatrick et al., 2019; Munro, 1989), while z_0 for smooth glacier ice surfaces (z_{0_ice}) typically range 350 between 0.1 and 6 mm (Brock et al., 2006). Munro (1989) measured z_0 values between 0.67 and 2.48 mm along and across the grain of the ice, respectively, and 5-6 mm for snow on nearby Peyto Glacier, which has a similar ice facies morphology as the Saskatchewan Glacier. A mean z_{0_ice} of 1.58 mm and z_{0_snow} of 5.5 mm were thus used in the model, with an uncertainty range of ±1 mm used for sensitivity analysis. The roughness length for temperature and water vapour were both considered to be two orders of magnitude less than roughness lengths for wind (Hock and Holmgren, 2005).

3.4 Model validation and parameter uncertainty

The simulated mass balance was validated at the point-scale against available seasonal and annual glaciological mass balance observations since 2012, and at the glacier scale using the reconstructed geodetic mass balance from 1979 to 2016. These data are described in detail in the Supplementary Material. While the physical nature of the model did not require formal calibration, four uncertain model parameters were subjected to sensitivity analysis to characterize the impact of their uncertainty on modelled mass balance. The precipitation lapse rate was varied within ± 4% 100 m^{-1} (c.f. section 3.2.2), ice albedo (α_{ice}) within ± 0.03 (c.f. section 3.3.2), and the aerodynamic roughness lengths for ice (z_{0_ice}) and snow (z_{0_snow}) within ± 1 mm (c.f. section 3.3.4). The sensitivity of simulated mass balance to NARR downscaling was also examined by forcing the model with the raw NARR inputs after adjusting the air temperature and precipitation for the elevation difference between the NARR gridpoint and the reference weather stations, using the mean calculated temperature and precipitation lapse rates (e.g. Fiddes and Gruber, 2014).

3.5 Climate sensitivity

The validated DEBAM model was used to perform a static (e.g. with fixed 2010 glacier geometry) climate sensitivity analysis of mass balance (Oerlemans, 2001) to potential changes in air temperature (ΔTa) ranging between 0 to 8 °C (1 °C interval) and precipitation (ΔP) ranging between -20 to +20% (5% interval). These warming and precipitation changes scenarios encompasse mean annual changes projected by ensemble GCM simulations for the mid (2041-2070) and late (2071-2100) 21st century relative to the most recent 30-year climatological period (1981-2010) and under different greenhouse gases emission scenarios (IPCC, 2013). The ensemble climate projections from the Coupled Model Intercomparison Project Phase 5 (CMIP5) were obtained from the KNMI Climate Change Atlas (Trouet and Van Oldenborgh, 2013) for Representative Concentration Pathway (RCP) scenarios +2.6 (n=32), +4.5 (n=42), +6.0 (n=25) and +8.5 (n=39) for the gridpoint closest to the ELA of Saskatchewan Glacier (Figure 1). The number of simulations depended on the availability of the CMIP5 models for each scenario (IPCC, 2013). The *IPCC AR5 Atlas* subset was used, which uses only a single realisation of each model and weights all models equally, where model realisations differing only in model parameter settings are treated as different models (IPCC, 2013). The DEBAM model was run 81 times for every combination of ΔTa and ΔP perturbation imposed on the *Ta* and *P* records over the 30-year reference period 1981-2010. Changes in mass balance for each sensitivity run were plotted as response surfaces, which provide a simple way to assess climate sensitivity across a range of possible climate change scenarios (e.g. Aygün et al., 2020; Prudhomme et al., 2010). Mean temperature and precipitation changes along with their 95% confidence intervals were overlained onto the response surfaces to show the most likely future climate trajectories given by the GCM projections.

4 Results

4.1 Meteorological observations

385

Daily and monthly averages of air temperature (Ta), relative humidity (RH), incoming solar radiation (G) and wind speed (WS) measured at the glacier AWS show notable differences between the two years of observation (Figure 2). The winter of 2014-2015 was, overall, colder than 2015-2016, with frequent cold excursions below -15 °C and a winter absolute minimum of -27 °C vs. -17 °C in 2015-16, although conditions were warmer in December. Relative humidity is generally high throughout

390
the year (mean = 79%), illustrating the predominantly humid climate of the Columbia Icefield, but decreases noticeably in summer. The variability in daily RH is similar between the two years of measurements. The incoming solar radiation shows pronounced seasonality, varying between ~50 W m^{-2} in winter and ~300 W m^{-2} in summer, with daily variations between 50 W m^{-2} in winter and 150 W m^{-2} in summer caused by variable cloud cover. The wind speed is generally high (mean = 16 m s^{-1}) and shows significant day-to-day variations, as well as higher values in winter. A gradual increase in wind speed is notably

395
observed from the lowest monthly mean value in May 2015 (6 m s^{-1}) to a maximum in February (26 m s^{-1}). The homogenized historical precipitation record from the Columbia Icefield and Parker Ridge stations contains several gaps but still displays the seasonal and interannual variability in precipitation near the glacier (Figure 2e). The mean monthly accumulated precipitation throughout the historical period is 73 mm month^{-1} (874 mm a^{-1}) but varies between 23 mm mo^{-1} (276 mm a^{-1}) and 142 mm mo^{-1} (1704 mm a^{-1}). Precipitation are more abundant in winter, with 58% of precipitation falling between October to March,

400
mostly as snow, and 42% falling during April-September, mostly as rain.
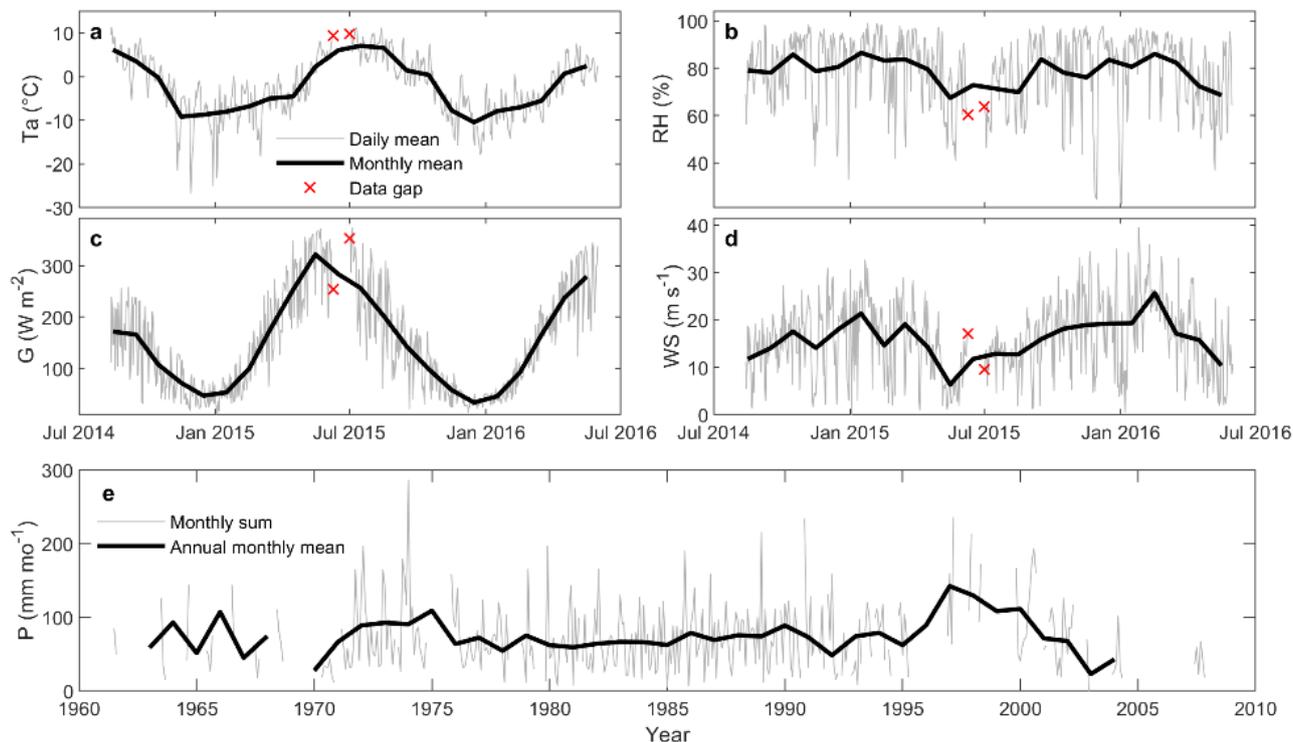
Figure 2. Two-year record from the Saskatchewan Glacier AWS (2014-2016). (a) Air temperature (Ta); (b) relative humidity (RH); (c) incoming global solar radiation (G); (d) wind speed (WS). The red crosses delineate the data gap caused by the fall of the AWS (11 to 30 June 2015). (e) Homogenized precipitation record from Parker Ridge and Columbia Icefield permanent stations.

4.2 NARR bias correction

The NARR meteorological variables used to drive the glacier mass balance model were compared with data from the glacier AWS (2014-16) and the 29-year long nearby homogenized daily precipitation record (Table 1). Results show that even without applying bias correction Ta, RH and G show a good correlation with the NARR data on a daily scale. As expected, the correlation is poorer for WS, likely because the local glacier katabatic wind recorded by the AWS is not well represented in NARR due to its coarse grid resolution. The NARR precipitation is also rather poorly correlated with observations. Biases in raw NARR variables are relatively small compared to the mean and range of values recorded (Figure 2), except for G (30.4 W m^{-2}) and precipitation (0.55 mm d^{-1}), which represent 15% and 25% of their mean measured values over their period of observation, respectively. The cold bias (-1.26 °C) observed for NARR Ta is consistent with the elevation difference between the AWS (2193 m) and the NARR gridpoint (2430 m) (ΔZ = 237 m), which results in an expected temperature difference of -1.19°C using the mean observed lapse rate of -0.5 °C 100 m^{-1} (c.f. Sect. 4.3). Neither the scaling nor the EQM correction methods improved the Pearson correlation coefficient (R) – primarily since R is a relative measure of the synchronicity between

420 two-time series and is unaffected by the mean values. The EQM method was found to improve Ta best, closely followed by the scaling method. Validation statistics were significantly improved using the scaling technique for precipitation and WS, while the diurnal scaling correction applied to G also reduced its errors. Both methods did not improve the errors in relative humidity, which had an initial low error. Overall, the scaling method was globally the more efficient approach across all variables and this method was thus applied to all variables for consistency, except for relative humidity, which remained uncorrected. Similar results, although with expectedly higher errors, were found for the interpolated NARR hourly data

425 (Supplementary Table S3).

Table 1. Statistical downscaling of NARR data using a two-year AWS record and the 29-year homogenized historical precipitation record. The daily validation is first done over the entire period before bias correction ('no downscale'). Validation statistics for each bias correction methods are the mean of the two left-out sub periods (see methods). R = Pearson correlation coefficient; RMSE = root mean square error; Bias = mean error (NARR minus observations); MAE = mean absolute error.

Method	Statistic	Ta (°C)	WS (m s⁻¹)	RH (%)	G (W m⁻²)	P (mm d⁻¹)
No downscale	R	0.98	0.37	0.85	0.92	0.30
	RMSE	1.94	2.30	7.96	52.72	5.22
	Bias	-1.26	-1.12	-0.09	30.41	0.55
	MAE	1.57	1.85	6.17	38.51	3.10
Scaling	R	0.98	0.37	0.85	0.93	0.30
	RMSE	1.49	2.21	7.97	39.08	4.96
	Bias	0.00	0.00	0.03	-0.25	0.00
	MAE	1.16	1.72	6.15	29.10	2.82
EQM	R	0.98	0.37	0.86		0.26
	RMSE	1.39	2.33	8.06		5.92
	Bias	0.03	0.01	-0.11		-0.03
	MAE	1.04	1.82	6.04		3.06

Monthly and annual averages of the bias-corrected NARR variables used to drive the mass balance model are displayed in Figure 3. There is no visible trend in mean annual Ta over the 30 years period except since 2010, but there is a noticeable

435 increase in minimum temperatures, with e.g., only two years with a monthly mean colder than -15 °C in 2000-2015 compared to seven years prior to 2000. The positive trend seen in mean annual RH is driven by increasing annual minima while annual maxima show no trend, and so the seasonal amplitude decreases over time. The monthly RH averages decrease in July and August (mean = 72%) while winter months have higher values (mean = 80-82%) (Figure 3b). No clear trends occur in annual cloud cover (CC) and G, despite the observed trend in RH (Figure 3d, f). The largest annual deviations in CC, e.g., after 2005,

440 are reflected by inverse fluctuations in G, reflecting the attenuation of solar radiation by clouds. A progressive decline in WS occurs from 1979, reaching the lowest annual value of the period in 1995 (~4.3 m s⁻¹) (Figure 3c). A more subdued increase in WS occurs afterward until 2010, followed by a decline. Finally, mean monthly precipitation shows no long-term trend but

significant seasonal and interannual variability (Figure 3e). The seasonal amplitude decreases after 2000, driven by increasing

seasonal minima and reduced maxima. A slight increasing trend in P is noted in the last part of the record, since ~2000.

445
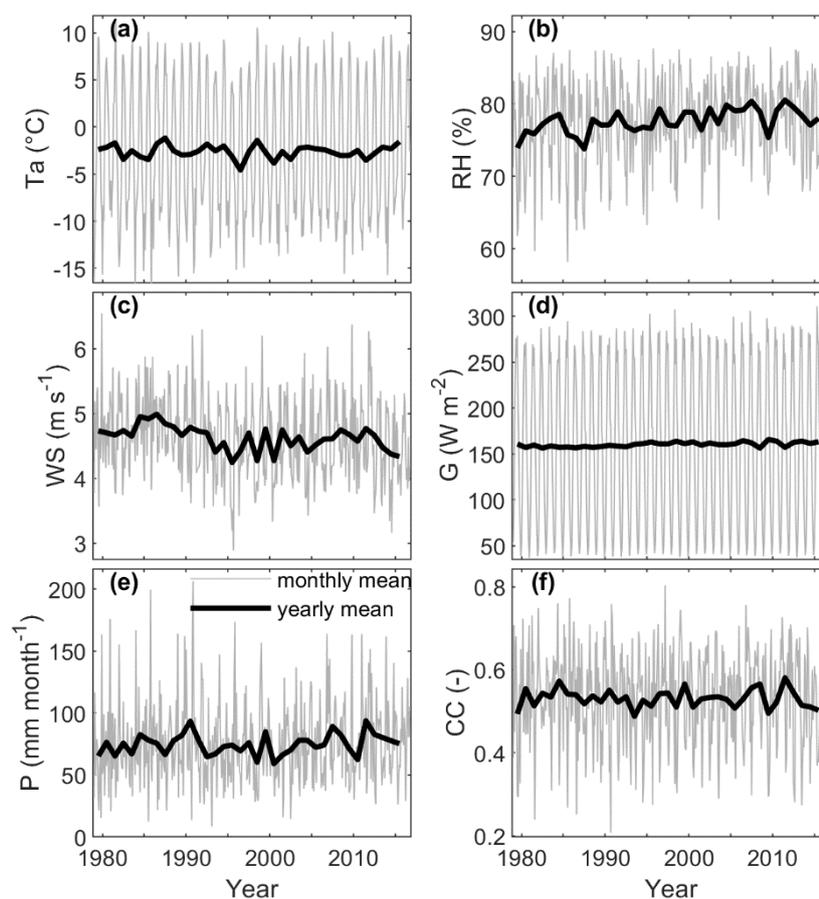
Figure 3. Downscaled NARR variables used to drive the DEBAM model. Grey solid lines represent monthly means and black solid lines represent annual averages.

450 **4.3 Air temperature lapse rates**

On-glacier diurnal air temperature lapse rates were found to vary between -0.55 °C 100 m⁻¹ at night and to increase during the

day, reaching a maximum of -0.34 °C 100 m⁻¹ at midday (Figure 4a). The strength of the temperature-elevation relationship,

as measured by the correlation coefficient (R), is generally high (R > 0.95) but decreases slightly during daytime hours

(R = 0.92). Notably, the lapse rates were constant at night due to the absence of sunlight effects on surface temperature, while

455 differential heating between the glacier tongue and the upper accumulation area and the associated local wind regimes

(katabatic vs. valley wind) could explain the partial breakdown of the relationship and smaller lapse rates during the day. While

wind speed increased during the day, katabatic winds prevailed, with little deviation of the wind direction within the day (Figure 4a). On a monthly scale, the lapse rate, calculated from seven stations from the permanent network, varied between -0.58 °C 100 m^{-1} and -0.42 °C 100 m^{-1} without any systematic seasonal pattern (Figure 4b). The correlation for the monthly

460   lapse rates is also more variable than for the diurnal lapse rates, varying between low values (R = 0.6) in winter to higher values (R = 0.94) in summer. The wind blows dominantly down-glacier (katabatic) with the relative wind direction showing a mixed contribution of the main accumulation area upwind of the AWS and the glacierized plateau North of the AWS. Mean diurnal lapse rate anomalies, calculated as deviations from the average on-glacier lapse rate in Figure 4a, were added to the monthly lapse rates (Figure 4b) and used to distribute air temperature to the glacier surface.

465
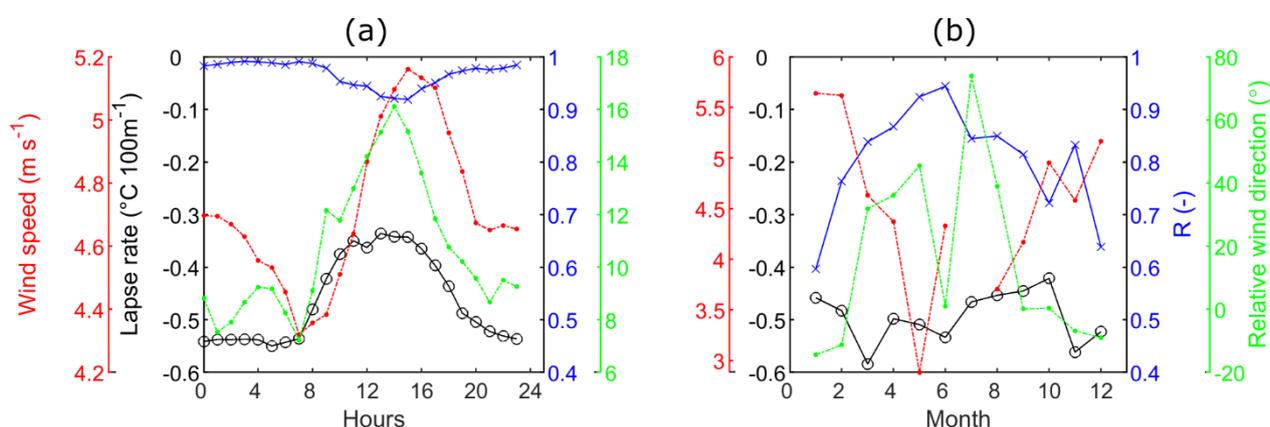
Figure 4. Calculated air temperature lapse rates. The black axis represents the air temperature lapse rate in °C 100 m^{-1}, the blue axis represents the correlation (R) between air temperature and elevation, the red axis represents wind speed and the green axis the wind direction relative to the main glacier axis (0° = up-glacier, 180° = down-glacier). (a) Diurnal temperature lapse rate from five
470   **HOBO^{TM} microloggers installed on ablation stakes from May to August 2015. (b) Seasonal variation of the lapse rate derived from seven permanent weather stations (see Figure 1). The wind data on both panels are from the glacier AWS.**

4.4 Model performance

4.4.1 Comparison with glaciological mass balance

475   The mass balance simulated with DEBAM was compared with glaciological mass balance observations available between 2012 and 2016. Overall, the seasonal and annual mass balance components are well simulated by the model, with most observations lying near the 1:1 line and with Nash-Sutcliffe Efficiency (NSE, Nash and Sutcliffe, 1970) coefficients of 0.84 for *bw* (n=49), 0.83 for *bs* (n=12) and 0.91 for *ba* (n=12) (Figure 5). Before the adjustment of the atmospheric emissivity calculation in the LWin equation (c.f. Sect. 3.3.3), the model tended to overestimate melt in the accumulation zone and

480   underestimate it in the ablation zone. The NSE was increased by 0.04 for *bw*, 0.07 for bs and 0.06 for *ba* after modifying the parametrisation. The modelled *bw* was underestimated in 2016 in the upper part of the glacier and overestimated in the lower

part, suggesting that the precipitation gradient for that year significantly differed from the other years. This shows one limitation of the model, which uses a constant, average precipitation lapse rate to distribute precipitation over the glacier surface. 2016 was a dry year, with the glacier AWS recording a small amount of snow accumulation during winter (AWS: 2015 = 135 cm, 2016 = 25 cm). Data from ablation stakes are more limited, and despite the overall good model performance, modelled *bs* and *ba* were slightly underestimated in 2014 and 2016 and overestimated in 2015 compared to the observations.

The simulated mass balance gradient compares generally well with observations for the three years with available *ba* measurements (Figure 5d). Overestimation of ablation at the two ablation stakes from 2014 is apparent, however leading to underestimated mass balance (*ba*) in the upper glacier for that year. The equilibrium line altitude (ELA) was ~2600 m for 2014-2016, which is near the average ELA of 2587 m simulated for the entire 1979-2016 period. The mean simulated mass balance gradient for the three validation years (2014-2016) was 0.98 cm w.e. m^{-1} in the ablation zone, with a steeper inflection below the ELA, and decreasing to 0.31 cm w.e. m^{-1} in the accumulation zone. Long-term values were 0.96 cm w.e. m^{-1} and 0.29 cm w.e. for 1979-2016, yielding a balance ratio (BR: the ratio of ablation to accumulation area balance gradients) of 3.34. This value is rather high, and closer to typical values (BR = 2.09 ± 0.93) for 'North America West Coast' glaciers which have a more humid climate than 'North America – Eastern Rockies' (BR = 1.11 ± 0.1) (Rea, 2009). This high value implies that a smaller ablation area is needed to balance inputs in the accumulation area (Benn and Evans, 2014).
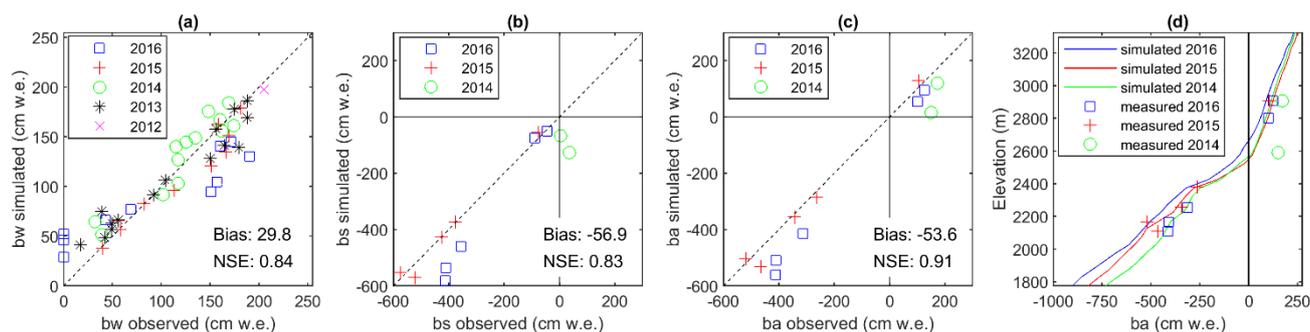
Figure 5. Simulated mass balance compared with point mass balance observations available between 2012 and 2016. (a) Winter balance (bw); (b) summer balance (bs, only available since 2014); (c) annual balance (ba). Mass balance is expressed in centimeters water equivalent (cm w.e.). The dashed line is the 1:1 relationship. (e) Simulated vs. observed annual mass balance gradient between 2014 and 2016.

4.5 Mass balance reconstruction and comparison with geodetics estimates

The simulated annual specific (glacier-wide) mass balance (*Ba*) was overall negative throughout the period (mean = - 0.72 m w.e. a^{-1}) with pronounced interannual variability (std = 0.57 m w.e. a^{-1}) (Figure 6a). The effect of dynamical adjustment on *Ba* was obtained as the difference between the dynamical simulation (multitemporal DEMs), which account for the dynamical response of the glacier, and the 1979 static simulation (fixed 1979 DEM). The effect was overall small from 1986 (first DEM

update) onward (mean = 0.06 m w.e. a^{-1}), but accelerated over the last 15 years (Figure 6a). The simulated mass balance with

510   the multitemporal DEMs is in good general agreement with the geodetic estimates (Figure 6b). The cumulative error if the geodetic estimates increases in 1999 due to the large error in the SRTM DEM, even though it was coregistered to the high-quality WV2 2010 DEM (supplementary material). The static simulation with the 1979 DEM, when the glacier was thicker and larger, results in a larger cumulative mass loss (~ -3 m w.e. over 37 years) than when using the 2010 DEM with the smallest historical extent. Essentially the larger extent in 1979 provides more area available for melting at lower altitudes. The dynamic

515   mass balance simulation remains between the limits of the two-endmember static simulations, with a difference in cumulative mass loss of ~ ± 1.4 m w.e at the end of the period.

4.6 Sensitivity to parameters uncertainty and NARR downscaling

Forcing the mass balance with raw NARR, after correcting Ta and P for the elevation difference between the NARR gridpoint and the reference weather station, resulted in a significant cumulative error in simulated *Ba,* with the cumulative *Ba* in 2016

520   being more negative by 15 m w.e. compared with the simulation with the bias-corrected NARR (Figure 6b). Results from the parameter sensitivity analysis show that the simulated mass balance is most sensitive to the uncertainty in the precipitation lapse rate (±4% 100 m^{-1}) followed by the ice aerodynamic roughness length (z_{0_ice}: ±1 mm) (Figure 6c). The sensitivity to uncertainties in ice albedo (α_{ice}: ±0.03) and the snow aerodynamic roughness length (z_{0_snow}: ±1 mm) were smaller and of similar magnitude (refer to the overlap of the coloured envelopes in Figure 6c). These results clearly show that a careful

525   assessment of the precipitation lapse rate and ice aerodynamic roughness length are needed to derive a reliable long-term mass balance reconstruction. Constraining these two parameters as well as the ice albedo and the snow aerodynamic roughness length against the observations is thus pivotal to replicating the recent direct mass balance observations (Figure 5) and long-term geodetic estimates (Figure 6).
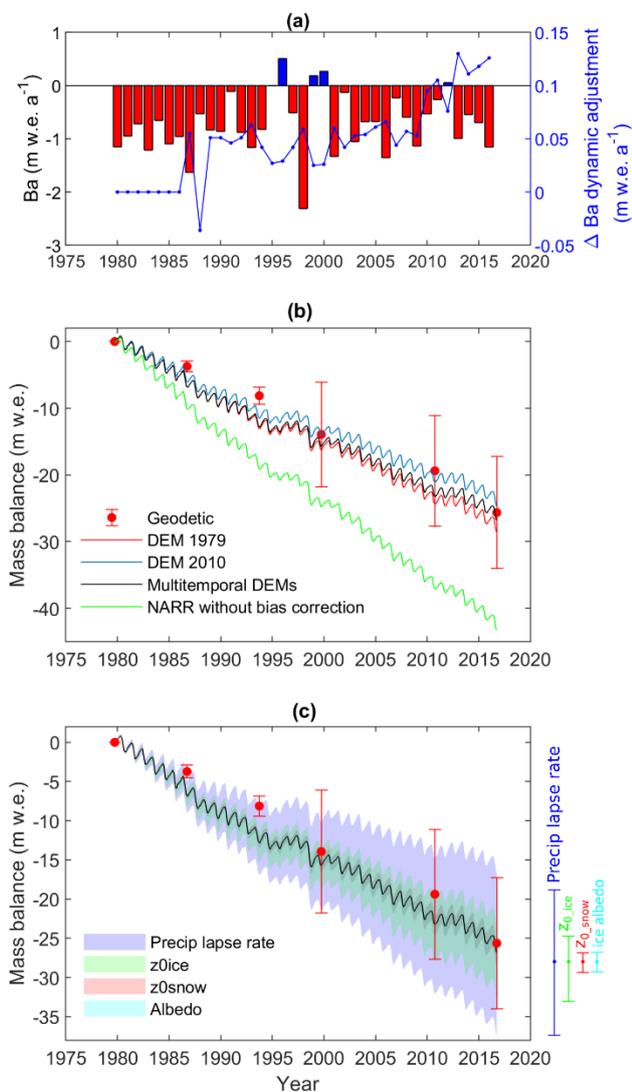
Figure 6. Simulated mass balance compared with geodetic estimates. (a) Annual glacier-wide mass balance (*Ba*) from the dynamical simulation (multitemporal DEMs). The blue curve represents the effect of dynamical adjustment on *Ba*. (b) Cumulative mass balance from static (red: 1979, blue: 2010) and dynamic (black: multitemporal DEM) simulations. Error bars represent one-sigma cumulative confidence intervals around the cumulative geodetic mass balance. The green trace represents the simulation forced with topographically-corrected NARR Ta and P, but without bias correction. (c) Sensitivity of simulated mass balance to parameter uncertainty. Coloured envelopes represent the cumulative uncertainty and the coloured error bars on the right show the effect of parameter uncertainty on the 1979-2016 cumulative mass balance.

4.7 Energy and mass fluxes

Monthly energy balance shows that the sensible heat flux (QS) dominates energy gains throughout most of the year (Figure
540   7). The contribution of QS is fairly constant throughout the year, increasing only slightly in July-August and decreasing slightly
in spring (March-May). The contribution of the net solar radiation flux (SW*) increases systematically from low values in
winter (November-February) when the sun angle is low and the glacier is covered by highly reflective snow, to peak values in
July-August when the sun angle is high and low-albedo ice is exposed in the ablation area. Only in July and August does the
net solar radiation (SW*) becomes the dominant energy source. The latent heat flux (QL) is small over Saskatchewan Glacier,
545   due to the generally high relative humidity (see Figure 2). QL is positive on average and highest in summer, reflecting the
predominance of deposition and condensation processes over sublimation. QL represents a small, but non-negligible (7%) heat
gain throughout the year, which reaches 11.5% in July-August. Energy loss occurs mainly by radiative cooling (LW*). Lower
air and surface temperature respectively reduce the incoming atmospheric longwave radiation and outgoing longwave
emissions from the glacier surface, thereby reducing LW* in winter. LW* increases somewhat in summer (June-August),
550   mainly because the glacier surface is near its melting point, limiting longwave radiation losses. The energy supplied by rain
(QR) has a negligible influence on the energy balance. Melting (QM) predominantly occurs between May and October and
peaks in July-August, due to the elevated SW*, QS and QL fluxes, and radiative cooling (LWout) limited by the melting
surface.
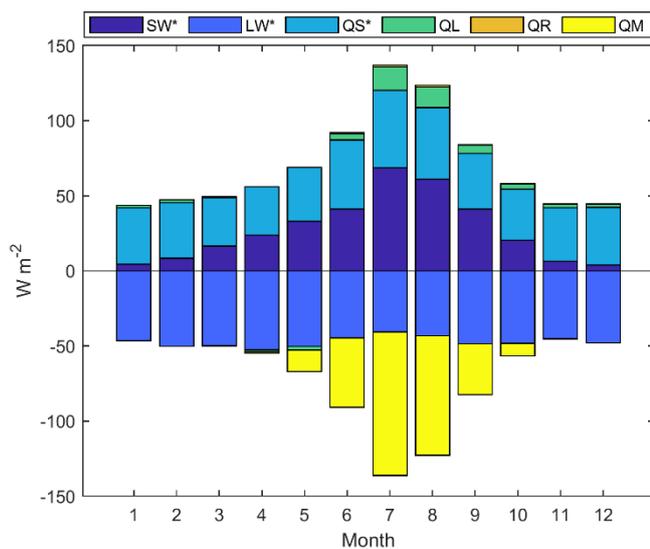
555

Figure 7. Mean seasonal cycle of simulated surface energy balance on Saskatchewan Glacier between 1979-2016 from the multi-temporal DEM simulation.

Four processes influence mass balance during the year (Figure 8a). Snowfall and snow accumulation dominate during the
560   accumulation season (October-April). Melt mainly occurs from May to October and peaks in July-August in response to the
positive surface energy balance (Figure 7). Deposition/condensation and sublimation fluxes are small. Net deposition
predominates while net sublimation occurs in the spring (April-June), when there is high incoming radiation and the upper
reaches of the glacier have not yet reached the melting point (Figure 8a). Although the QL heat flux was found to be non
negligible during summer (Figure 7), the resulting mass loss is itself negligible compared to melting because the latent heat of
565   sublimation/deposition is seven times larger than that for melting. Moreover, the latent heat flux has a pronounced diurnal
cycle, switching from deposition at night when cooling of moist air causes the vapour pressure to increase relative to the
melting glacier surface, while daytime heating reverses the vapour gradient between the glacier surface and the atmosphere,
causing sublimation (Figure 8b). Hence the two regimes tend to compensate each other. Nevertheless, the nighttime deposition
slightly dominates daytime sublimation, leading to a net positive deposition/condensation flux on average to the glacier surface.
570
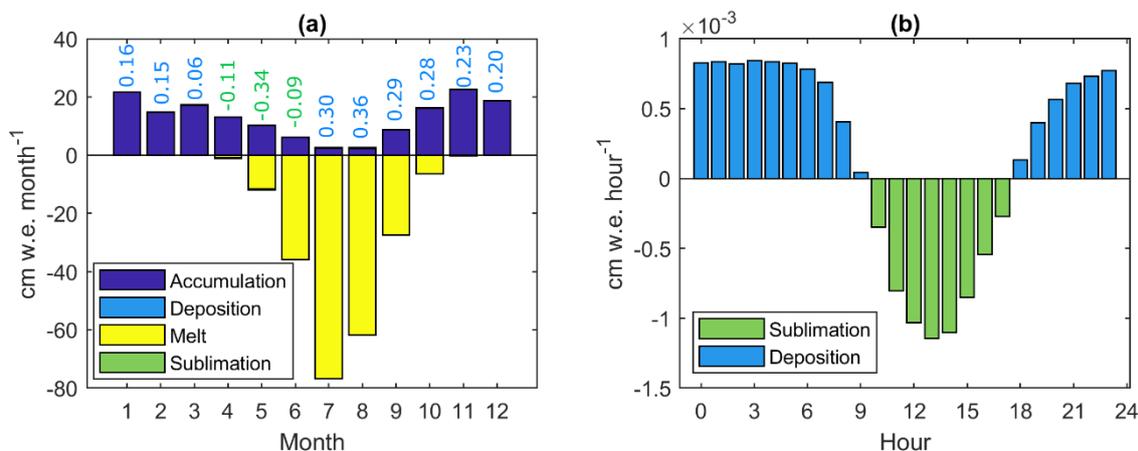
Figure 8. Mean simulated mass fluxes on Saskatchewan Glacier between 1979-2016 using multi-temporal DEM. (a) Mean monthly fluxes; deposition and sublimation fluxes being much smaller they are also indicated as numbers (cm w.e. month $^{-1}$). (b) Mean diurnal cycle in deposition/condensation and sublimation.

575

Simulated spatial mass balance patterns (Figure 9) show an annual snowfall average of 154 cm w.e over the glacier with a
minimum of 30 cm w.e near the toe to ~300 cm w.e over the upper reaches. Annual ice melt can reach 786 cm w.e. a^{-1} at the
glacier margin and 54 cm w.e. a^{-1} in the upper accumulation zone. Net deposition/condensation predominates on average over
the glacier, but fluxes are small (< 3 cm w.e. a^{-1}), while net sublimation only occurs on the upper reaches of the glacier, mostly
580   in the Spring (Figure 9c, Figure 8a), corresponding to areas with high incoming solar radiation (Supplementary Figure S4). On
average, melting losses (mean = -222 cm w.e. a^{-1}) exceed snow precipitation gains (+154 cm w.e. a^{-1}) and the small
condensation gain (mean = +1 cm w.e. a^{-1}), yielding a mean negative annual balance (-67 cm w.e. a^{-1}).
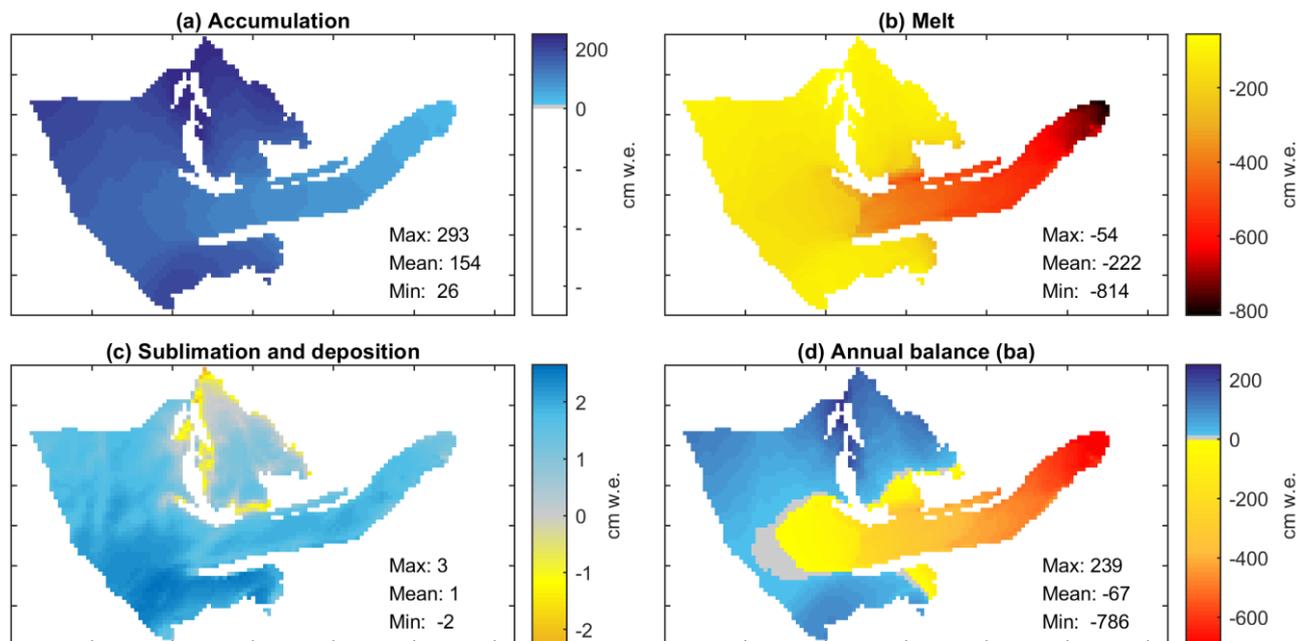
 Figure 9. Simulated spatial patterns of annual mass balance (cm w.e.) on Saskatchewan Glacier between 1979-2016. (a) Snow accumulation; (b) melt; (c) sublimation and deposition; (d) annual balance. The accumulation zone on (d) is delineated by the positive blue colour scale, the ablation zone by the negative yellow/red scale and the area of neutral balance in grey (*ba* = 0).

4.8 Climate sensitivity analysis

The static sensitivity of mean mass balance (*B*) components to various climate perturbations (ΔTa = 0 to +7 °C and ΔP = -20

590 to +20%) was examined using the 2010 DEM as reference glacier geometry (Figure 10). The reference scenario (1981-2010) yields an average annual mass loss (*Ba*) of -0.68 m w.e. a^{-1} (Figure 10c). The response surface for *Ba* shows that the glacier-wide mass balance is sensitive to changes in air temperature, and much less sensitive to changes in precipitation (Figure 10c). The ΔBa contours also become steeper and narrower with increased warming, which indicates a reduced sensitivity to precipitation and increased sensitivity to temperature, respectively. The seasonal mass balance response sufaces help to

595 understand the *Ba* sensitivities (Figure 10a,b). The *Bw* response surface shows that a precipitation increase of +20% can buffer the negative impact of warming on *Bw* up to +3 °C of warming, but up to +0.5 °C only for *Ba*. Moreover, a warming of more than +6 °C with no change in precipitation would supress net accumulation in winter, given the current glacier extent (2010) (Figure 10a). The sensitivity of winter mass balance to temperature changes also increases markedly with warming, as seen by the progresive tightening of the contours in Figure 10a. This is interpreted to result from decreasing accumulation due to the

600 increasing shift from snowfall to rainfall and increased ablation during winter (Oct.-April) due to earlier disapearance of the snow cover under more pronouced warming. Conversaly, the temperature sensitivity of summer mass balance (*Bs*) increases only slightly with the warming scenario, and the steep contours in Figure 10b suggest a small sensitivity to precipitation

changes. The increased temperature sensitivity of *Ba* with warming indicated in Figure 10c is therefore mainly attributed to decreasing accumulation from reduced snowfall fraction and increased winter ablation as the climate warms and the snow

605 cover retreats up-glacier earlier in the Spring (Figure 10a).

IPCC RCP scenarios for the mid (2041-2070) and late (2071-2100) 21st century were overlapped onto the response surfaces to show the most likely future climate trajectories given by the latest projections from climate models. The RCP projection have significant uncertainities, as shown by their wide 5-95% confidence intervals and the annual mass balance change can

610 vary by as much as ±3 m.w.e. a^{-1} within a single scenario. This illustrates the usefulness of scenario-free response surfaces to assess glacier mass balance sensitivity to climate as a background to evolving climate projections (Aygün et al., 2020; Prudhomme et al., 2010). Nontheless, given the current ensemble climate scenarios the (static) mass balance could decrease by -0.5 to -2.0 m w.e a^{-1} by the mid-century, and by -0.5 to -4 m w.e a^{-1} by the end of the century, relative to baseline conditions (*Ba* = -0.68 m w.e. a^{-1}) and depending on the RCP scenario considered.

615
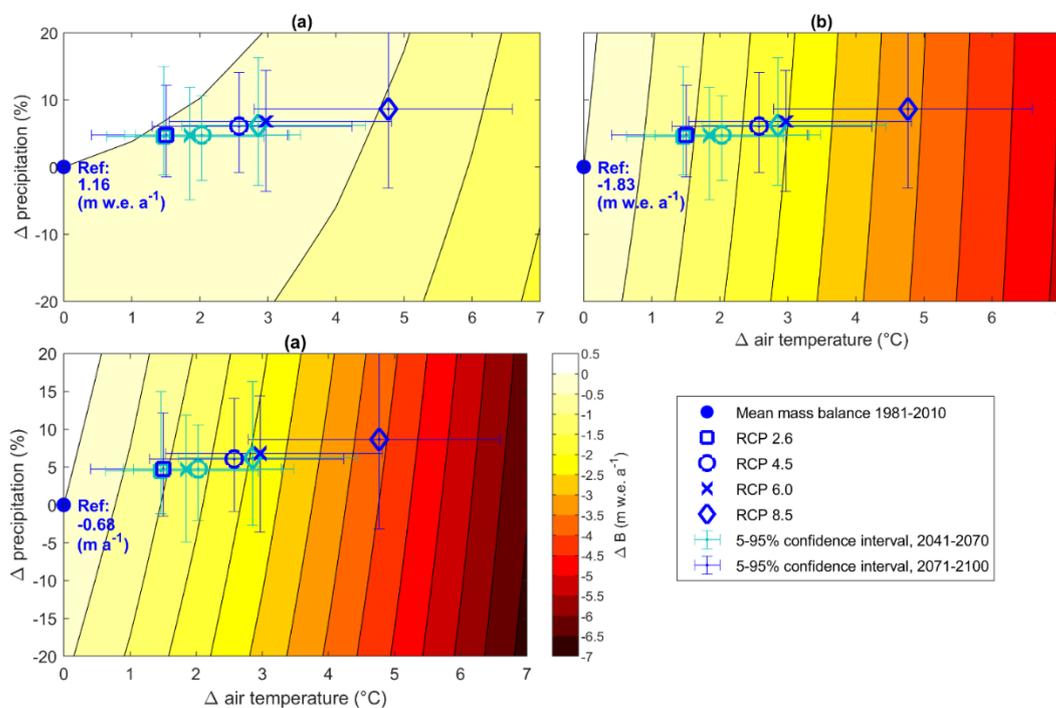
Figure 10. Static (2010 DEM) mass balance sensitivity to prescribed changes in regional mean air temperature between 0 to 7 °C and precipitation between -20 to +20%, which encompass IPCC representative concentration pathways (RCP) ensemble scenarios +2.6, +4.5, +6.0 and +8.5 for the mid (2041-2070: dark blue) and late (2071-2100: light blue) 21st century. The mean seasonal and
620 **annual mass balance are shown for the reference period 1981-2010. (a) Winter balance (*Bw*); (b) summer balance (*Bs*); (c) annual balance (*Ba*).**

Since *Ba* displays a large sensitivity to temperature and because glacier melt is the outcome of complex glacier-atmosphere energy exchanges, the sensitivity of energy and mass fluxes to warming was further investigated (Figure 11). Under warming
625   scenarios with no changes in precipitation, a more negative mass balance response is dominated by increased melting (~93%), while increasing condensation accounts for ~ -3% (mass gain) of the net annual mass changes in response to warming (Figure 11a, b). Warming alters the precipitation phase, with the snowfall ratio decreasing non-linearly from 0.80 under present climate to 0.47 at ΔTa +7°C (Figure 11c). This progressive conversion from snowfall to rainfall accounts for ~10 % of the mass changes in response to warming (Figure 11b).

630

The total energy input to the glacier surface increases with warming temperatures, and the increased energy is predominantly used for melting (QM), which shows a non-linear increase with respect to warming (Figure 11d, e). Interestingly, the increase in energy supply with warming is mainly driven by an increase in net solar radiation (SW*) and latent heat flux (QL), with more subdued increases in the temperature-dependent sensible heat (QS) and net longwave radiation fluxes (LW*) (Figure
635   11e). Since cloud cover remained unchanged in the sensitivity experiments, the increase in SW* with warming is entirely driven by the decreasing albedo as snow cover duration on the glacier decreases (Figure 11c). Since the relative humidity also remains constant in our sensitivity analyses, and because warming increases the saturated vapor pressure of the air, warming leads to higher atmospheric vapor pressures. Since the glacier surface is contrained to the melting temperature (0 °C) during a large part of the year, the increase in surface saturated vapor pressure in response to warming will, on average, be less than
640   that of the atmosphere, causing the vapor pressure gradient to increase and boost QL fluxes (deposition) to the surface. Similar reasoning applies to QS, i.e., the near surface temperature gradient will increase in response to atmospheric warming. While the rainfall ratio increases with warming, its influence on the energy balance is insignificant, but the reduced snowfall greatly impacts winter accumulation (Figure 10a). Increasing net solar radiation (SW*) contributes from 51% to 42% of the increase in QM (ΔQ), with the contribution decreasing with warming. The QL contribution to ΔQ increases from 27 to 29% in response
645   towarming, while that of LW* increases from 5 to 9%. The contributions of QS (~19%) and QR (~1%) are more constant (Figure 11f).
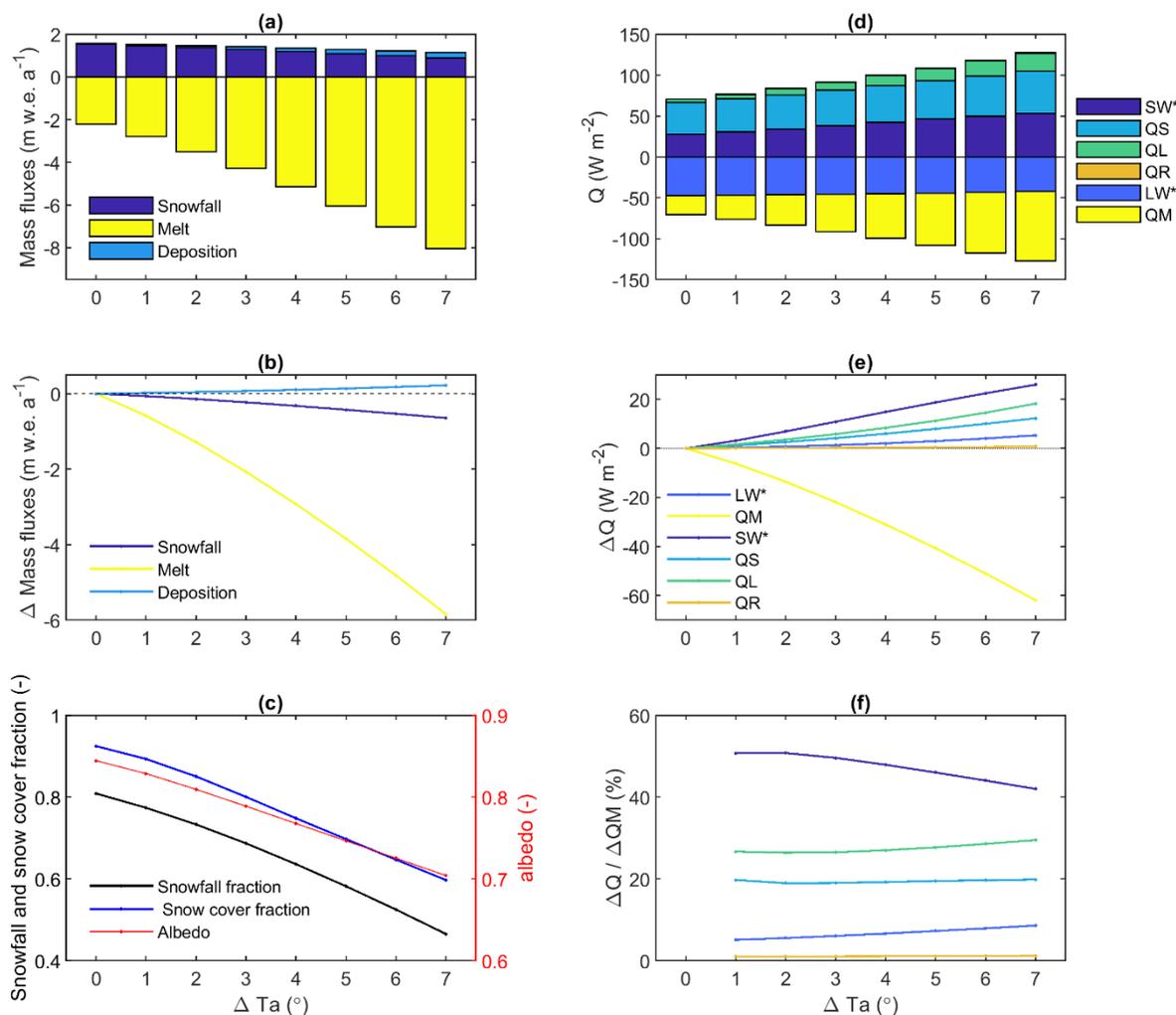
Figure 11. Static mass and energy balance sensitivity to changes in regional mean air temperature between 0 to 7 °C. (a) Mass balance; (b) changes in mass balance relative to baseline (Δ Ta = 0); (c) changes in snowfall to total precipitation ratio, snow cover, and albedo; (d) energy balance; (b) changes in energy balance relative to baseline (Δ Ta = 0); (e) Changes in energy fluxes scaled by the changes in melt energy (Qm). All fluxes and variables represent mean annual values averaged over the whole glacier surface and over the baseline 1981-2010 period with mean air temperature perturbed from 0 to 7 °C.

5 Discussion

5.1 Suitability of NARR for model forcing

The present study focused on reconstructing the mass balance of a glacier using a physically-based model constrained by a sparse set of glacio-meteorological data without calibration. This situation is common to many mountain glaciers of the world where logistical and financial constrains preclude continuous monitoring programs. In this context, the outputs of reanalysis

or numerical weather models represent an attractive alternative for driving glaciological models. The NAAR reanalysis
660   product, with its high spatial (32 km) and temporal (3-hourly) resolution can provide accurate meteorological information,
especially for 2 m temperature and 10 m wind in comparison with other global reanalysis datasets (Mesinger et al., 2006).
Several studies have used NARR to force hydrological and glaciological models in mountainous region using simple statistical
downscaling (Clarke et al., 2015; Ebrahimi and Marshall, 2016; Hofer et al., 2010) or dynamical downscaling (Arritt and
Rummukainen, 2011; Erler et al., 2015; Giorgi, 2006). While dynamical downscaling does not introduce additional
665   uncertainties associated with statistical calibration, the technique is computationally intensive (Mölg and Kaser, 2011). The
quality of meteorological observations used for statistical downscaling, however, will determine the quality of the downscaling
results, due to the necessary calibration step. In our study, the comparison between NARR and observations was reasonably
good given the short AWS record used for comparison. Even without downscaling, three variables (Ta, RH, SWin) showed
good correlation (R > 0.85) between NARR and AWS observations, and the simple scaling bias correction removed much of
670   the biases present. Moreover, the cold bias in NARR air temperature was consistent with the elevation difference between the
AWS and the NARR grid point and local temperature lapse rate. The low bias and high correlation for NARR air temperature
and relative humidity, and SWin to a lesser extent (Table 1), are consistent with previous findings from Trubilowicz et al.
(2016) who showed that these variables agree well with measured values at high-elevation stations in the southern Coast
Mountains of British Columbia, Canada. Wind speed (WS) was however poorly represented, most probably because thermal
675   winds (katabatic and valley winds) are not represented at the coarse 32×32 km spatial resolution of the NARR (Dadic et al.,
2010). Trubilowicz et al. (2016) also reported lower and site-dependent accuracy for NARR wind speeds. More sophisticated
wind downscaling (e.g. Vionnet et al., 2021; Wagenbrenner et al., 2016) could help improve further modelling at this site and
other upland icefield-outlet valley glacier settings.

680   The positive bias in NARR precipitation appeared consistent with the higher elevation of the NARR grid point relative to the
homogenized precipitation record (Table 1). However, once the effect of the elevation difference is corrected using the
calibrated precipitation lapse rate (15.6% 100 m^{-1}), the NAAR is found to underestimate observations by 10%. This is
consistent with the recent study by Hunter et al. (2020) who showed that NARR underestimates precipitation in the mountain
regions of British-Columbia, Canada. The NARR precipitation also correlated poorly with the off-glacier daily historical
685   precipitation record (R = 0.30), showing that the daily variability in NARR precipitation is not well represented. Precipitation
is notoriously more difficult to represent in reanalysis products, especially in complex terrain with steep orographic gradients
and localized convective activity (Hofer et al., 2010; Mesinger et al., 2006). Ebrahimi and Marshall (2016) also reported that
the NARR precipitation for the Haig Glacier, also in the Canadian Rocky Mountains, poorly represents the observed winter
accumulation totals. Nevertheless, NARR precipitation has been found to be reliable at the monthly scale and to represent a
690   useful input for hydrological modelling in North America generally (Chen and Brissette, 2017). Our results suggest this finding
also applies for glaciological modelling, given that bias-correction is applied. The underestimation of precipitation in NARR
combined with the positive bias in the raw global radiation mostly explain the exaggerated mass loss simulated by the mass

balance model when forced with the biased NARR (Figure 6b). More elaborate topographic corrections of solar radiation (Fiddes and Gruber, 2014) could improve the downscaling of NARR solar radiation in the absence of ground observations,

695   but precipitations biases remain difficult to correct in this situation.

5.2 Model performance and parameter sensitivity

Despite some simplistic model assumptions, the primary one being a constant precipitation lapse rate, the interannual variability in mass balance was relatively well simulated by the model, with NSE values of 0.83 to 0.91 for direct point observations (Figure 5). Point mass balance measurements with the glaciological method are affected by several uncertainties

700   related to errors in ablation stake height measurements, stake self-drilling into the ice or firn and snow/firn density measurements (Zemp et al., 2013). Errors in point measurements can range from 14 cm w.e. a^{-1} for ablation measurements on ice, 27 cm w.e. a^{-1} for ablation measurements on firn and 21 cm w.e. a^{-1} for snow measurements in the accumulation area (Thibert et al., 2008). The root-mean-squared-error (RMSE) on the simulated bw is 24.2 cm w.e. a^{-1} – on the same order as the typical measurement error for snow and firn. RMSE values, however, are higher than typical measurement errors for bs (87.0

705   cm w.e. a^{-1}) and ba (77.6 cm w.e. a^{-1}), due in part to the restricted number of available observations for validation (Figure 5). The reconstructed mass balance also compared favorably against the independent geodetic estimates (c.f. sect. 4.5, Figure 6). The cumulative mass loss was close to the geodetic estimates, despite the large uncertainties in the geodetic balance introduced from 2000 onward due to vertical uncertainties in the SRTM DEM. The long-term consistency between geodetic and modelled mass balance gives further confidence that the bias-corrected NARR forcings do not suffer from systematic biases.

710

The model sensitivity to uncertain model parameters showed that the simulated mass balance was most sensitive to uncertainties in the precipitation lapse rate, followed by the ice aerodynamic roughness, while the sensitivity to the snow aerodynamic roughness and ice albedo were lower. This demonstrates that the precipitation lapse rate must be carefully evaluated using ancillary meteorological data, which can be difficult in regions with no permanent weather station network

715   nearby. A high sensitivity to the ice aerodynamic roughness has been reported in several studies (e.g. Brock et al., 2000; Hock and Holmgren, 1996; MacDonell et al., 2013; Munro, 1989). It remains one of the most challenging parameters to constrain in glacier models, and the assumption of a spatially and temporally constant z_0 value is a simplistic representation of reality (Fitzpatrick et al., 2019). This parameter is indeed often calibrated in the absence of direct observations (Hock, 2005). In this study, observations from the nearby Peyto Glacier allowed using a representative value which yielded good results; however

720   the uncertainty range in the values reported by Munro (1989) ($\pm$ 1 mm) was sufficient to induce a $\pm$ 17% error in the simulated cumulative balance (Figure 6c). Advances in deriving aerodynamic roughness from remote sensing could help in the future to improve the calculation of turbulent fluxes in distributed glacier models (Chambers et al., 2020; Fitzpatrick et al., 2019; Smith et al., 2020). The use of remotely sensed albedo maps also contributed to constrain a representative value for ice albedo (c.f. 3.3.2) and the simulated mass balance was not very sensitive to the uncertainty around this estimate (Figure 6c). Nevertheless,

725 only an average value was used, when in fact significant heterogeneity was found within the ablation zone (supplementary material). Decreasing ice albedo can occur over the course of the melt season due to impurities of geogenic origin concentrating at the surface (Cuffey and Paterson, 2010), cryoconite development (Takeuchi et al., 2001) and more discrete events not taken into account in the model, such as algal mat development (Lutz et al., 2014) or wildfires that bring black carbon and ash onto the glacier and decrease the albedo (Marshall and Miller, 2020). Long-term darkening has also been observed on glaciers of

730 the European Alps, which questions the use of fixed albedo values in historical and future mass balance simulations (Oerlemans et al., 2009). Further efforts could look to assimilate such remotely sensed albedo maps within distributed models.

5.3 Impact of glacier recession on mass balance

The multi-temporal DEMs used in the study allowed quantifying the impact of glacier elevation changes on long-term mass balance (Figure 6). The dynamic mass balance simulation with the multitemporal DEMs showed a maximum difference in

735 cumulative mass balance of ~1.5 m w.e., or 5.6% of the static cumulative balance. This is a small difference overall, which shows that glacier recession has had a minor impact on the mass balance of Saskatchewan Glacier. This is expected, for this setting in particular, since the glacier margin is at the bottom of the occupying valley and glacier retreat has occurred over a restricted altitude range – thereby limiting negative feedback effects between glacier retreat and mass balance. This study has focused on the static climate sensitivity of mass balance, ignoring future dynamical feedbacks. Static, or 'reference' mass

740 balances calculated over a constant glacier hypsometry have been proposed to be better suited for climatic interpretation (Elsberg et al., 2001; Harrison et al., 2009). But from a hydrological perspective, future glacier retreat towards higher elevations would mitigate an increasing portion of the simulated mass loss, gradually increasing the difference between the static (2010 surface) and dynamical mass balance, and progressively decreasing the volume of meltwater released annually (Huss and Hock, 2018; Huss et al., 2012). An increase in dynamical adjustments effects on mass balance is already visible on

745 Saskatchewan Glacier from 2000 onward (Figure 6a).

5.4 Climate sensitivity

The simulated mass balance sensitivity to a +1°C warming was -0.65 m w.e. °C^{-1}. This value is comparable to other mid-latitude glaciers: -0.60 m w.e. °C^{-1} for the Illecillewaet Glacier in the Selkirk Mountains of British Columbia (Hirose and

750 Marshall, 2013), -0.66 m w.e. °C^{-1} for the Haig Glacier in the Canadian Rocky Mountains (Ebrahimi and Marshall, 2016), -0.65 ±0.05 m w.e. °C^{-1} for small (<0.5 km^2) glaciers in Switzerland (Huss and Fischer, 2016), -0.60 m w.e. °C^{-1} for the larger Morteratschgletscher, Switzerland (Klok and Oerlemans, 2004), and -0.61 m w.e. °C^{-1} for Storglaciären, Sweden (Hock et al., 2007). Higher sensitivities are found in more humid climates, e.g. -0.86 m w.e. °C^{-1} for the South Cascade Glacier, Washington (Anslow et al., 2008) and up to -2.0 m w.e. °C^{-1} on Brewster Glacier, New Zealand (Anderson et al., 2010), and lower

755 sensitivities in drier climate, e.g. -0.44 m w.e. °C^{-1} on Urumqi River Glacier No.1 in the Chinese Tien Shan (Che et al., 2019). Earlier work by Braithwaite (2006), Oerlemans and Fortuin (1992) and Oerlemans (2001) showed that the mass balance

sensitivity to temperature scales with mean annual precipitation, due to larger albedo and precipitation phase feedbacks and longer melt seasons on glaciers in wetter climates.

760   We find that the sensitivity of Saskatchewan Glacier mass balance to warming is dominated by increased melting (~90%) while the precipitation phase feedback only accounts for ~10%. We further find that the albedo feedback represents the main contributor to the temperature sensitivity for the Saskatchewan Glacier. Increases in net shortwave radiation caused by a reducing snow cover and ensuing decreased glacier albedo account for 42-51 % of the increase in melt energy across the various warming scenarios. A similar finding was reported on Haig Glacier by Ebrahimi and Marshall (2016), who found that

765   introducing albedo feedbacks doubles the net energy sensitivity to warming. This value is significantly high, but less than the 80% reported recently by Johnson and Rupper (2020) for the summer-accumulation type Chhota Shigri Glacier in High Mountain Asia. As shown by Fujita (2008), higher sensitivities are found for glaciers located in a summer-precipitation climate, where albedo feedbacks on ablation are stronger, than for glaciers located within a winter-precipitation climate.

770   For the Saskatchewan Glacier, a significant air humidity feedback was also found, with latent heat fluxes contributing 27-29% of the increased melting under warmer temperatures. Keeping the relative humidity constant under warming scenarios may be plausible for the high elevation Columbia Icefield. The icefield receives moist air from the British Columbia interior and the Pacific Ocean uplifted onto the icefield, as the region is subject to upslope conditions derived from convergent upper air masses as low-pressure systems spin by south of the region. Other glaciers subjected to subsiding air masses could experience drier

775   weather in the future, which would decrease their melt sensitivity to warming (Ebrahimi and Marshall, 2016). The large contribution of latent heat fluxes to melting under warming scenarios points to the necessity of considering changes in specific air humidity when simulating glacier melt under future climates. This conclusion is in line with the recent findings by Harpold et al. (2018) who showed that atmospheric humidity plays a critical role in local energy balance and snowpack ablation under warmer climates, with latent and longwave radiant fluxes cooling the snowpack under dry conditions and warming it under

780   humid conditions.

The mass balance sensitivity of Saskatchewan Glacier to a ±10% change in precipitation under the current temperature regime was 1.01 (m w.e. of mass change per m w.e. of precipitation change). A value of 1 would occur if all precipitation were snowfall and there were no albedo feedbacks on Ba (Oerlemans, 2001). Under the present climate, the snowfall fraction is 0.81

785   (Figure 11c), and thereby the albedo feedback on ablation contributes 0.20 to the mass balance sensitivity to precipitation. With the mean annual precipitation on the glacier being 1880 mm for the 1981-2010 reference period, the maximum +20% precipitation increase projected from ensemble climate scenarios for the end of the century would add a maximum of 0.4 m w.e. a^{-1}, which is small compared to the temperature sensitivity of -0.65 m w.e. °C^{-1}. As such, precipitation increases can only buffer up to +0.5 °C^{-1} of warming on Saskatchewan Glacier. As warming causes snowfall to shift to rainfall at a rate of ~ 5%

790   °C^{-1} (Figure 11c), this limits the buffering effect of increasing precipitation under warming scenarios, and accounts for 0.1 m w.e. °C^{-1} of the mean temperature sensitivity.

6 Conclusions

Despite their physical basis, energy-balance models often struggle to replicate mass-balance observations, due to the difficulty in constraining their numerous parameters and obtaining reliable meteorological forcings (Gabbi et al., 2014; Réveillet et al.,

795   2018). Our study showed that a physically-based, distributed mass balance model forced by reanalysis data can adequately reproduce the recent and long-term evolution of glacier mass balance when forcings and key model parameters are judiciously constrained with available observations and ancillary data. This is a key requirement for the effective application of such models, since parameters from distributed energy balance models dot not transfer well between sites (MacDougall and Flowers, 2011). While reanalysis data can provide realistic climate forcings for glacier models, bias-correction with in situ observations

800   remains desirable. Adopting this approach, however, requires a significant amount of work, which would be hard to implement at the mountain range scale.

The reconstructed mass balance of Saskatchewan Glacier shows a cumulative loss of -26.7 m w.e. over the period 1979-2016, in good agreement with independent geodetic estimates. Climate sensitivity experiments showed that future changes in

805   precipitation would have a small impact on glacier mass-balance, while the temperature sensitivity increases with warming, from -0.65 to -0.93 m w.e. °C^{-1}. Increased melting accounted for 90% of the temperature sensitivity while precipitation phase feedbacks accounted for 10%. Roughly half of the melt response to warming was driven by reductions in glacier albedo as the snow cover on the glacier thins and recedes earlier in response to warming (positive albedo feedback), while about one quarter of the response was driven by latent heat energy gains (positive humidity feedback). Our study underlines the key role of

810   albedo and air humidity in modulating the response of winter-accumulation type mountain glaciers and upland icefield-outlet glacier settings to climate.

7 Code availability

The glacier mass balance model code is available at https://regine.github.io/meltmodel/

8 Data availability

815   Downscaled NARR forcings, geodetic mass balance estimates and reconstructed mass balance are available from the corresponding author.

9 Author contribution

Conceptualisation: CK, MND. Formal analysis: OL, CK; Supervision: CK; Data Curation: MND, BM; Writing – original draft preparation: OL, CK; Writing – review & editing: CK, OL, MND, BM.

820 ## 10 Competing interests

The authors declare that they have no conflict of interest.

11 Acknowledgements

CK was supported and funded by the Fonds de recherche du Québec – Nature et Technologies, the National Sciences and Engineering Research Council of Canada and the Canada Research Chair Program. MND was supported and funded by Natural
825 Resources Canada's Climate Change Geoscience Program and the NSERC-CCAR Changing Cold Regions Network (CCRN). The authors thank Steve Bertollo, Eric Courtin, May Guan, Gabriel Meunier-Cardinal and Anthony Pothier-Champagne for assisting with field data collection. Jasper and Banff National Parks of Canada are thanked for supporting this work under Permit JNP-2010-4694.

12 References

830 Anderson, B., Mackintosh, A., Stumm, D., George, L., Kerr, T., Winter-Billington, A., and Fitzsimons, S.: Climate sensitivity of a high-precipitation glacier in New Zealand, Journal of Glaciology, 56, 114-128, 2010.
Anderson, S. and Radić, V.: Identification of local water resource vulnerability to rapid deglaciation in Alberta, Nature Climate Change, 10, 933-938, 2020.
Anslow, F. S., Hostetler, S., Bidlake, W. R., and Clark, P. U.: Distributed energy balance modeling of South Cascade Glacier,
835 Washington and assessment of model uncertainty, Journal of Geophysical Research: Earth Surface, 113, 2008.
Arnold, N., Willis, I., Sharp, M., Richards, K., and Lawson, W.: A distributed surface energy-balance model for a small valley glacier. I. Development and testing for Haut Glacier d'Arolla, Valais, Switzerland, Journal of Glaciology, 42, 77-89, 1996.
Arritt, R. W. and Rummukainen, M.: Challenges in regional-scale climate modeling, Bulletin of the American Meteorological Society, 92, 365-368, 2011.
840 Aygün, O., Kinnard, C., and Campeau, S.: Impacts of climate change on the hydrology of northern midlatitude cold regions, Progress in Physical Geography: Earth and Environment, 0, 0309133319878123, 2019.
Aygün, O., Kinnard, C., Campeau, S., and Krogh, S. A.: Shifting Hydrological Processes in a Canadian Agroforested Catchment due to a Warmer and Wetter Climate, Water, 12, 739, 2020.
Bamber, J. L., Westaway, R. M., Marzeion, B., and Wouters, B.: The land ice contribution to sea level during the satellite era,
845 Environmental Research Letters, 13, 063008, 2018.
Barnett, T. P., Adam, J. C., and Lettenmaier, D. P.: Potential impacts of a warming climate on water availability in snow-dominated regions, Nature, 438, 303-309, 2005.
Benn, D. and Evans, D. J.: Glaciers and glaciation, Routledge, 2014.
Bolch, T., Menounos, B., and Wheate, R.: Landsat-based inventory of glaciers in western Canada, 1985–2005, Remote Sensing
850 of Environment, 114, 127-137, 2010.

Bonekamp, P. N., de Kok, R. J., Collier, E., and Immerzeel, W. W.: Contrasting meteorological drivers of the glacier mass balance between the Karakoram and central Himalaya, Frontiers in Earth Science, 7, 107, 2019.

Braithwaite, R. J.: Measuring and Modelling the Mass Balance of Glaciers for Global Change. In: Glacier Science and Environmental Change, 2006.

855 Braithwaite, R. J. and Raper, S. C.: Glaciers and their contribution to sea level change, Physics and Chemistry of the Earth, Parts A/B/C, 27, 1445-1454, 2002.

Brock, B. W., Willis, I. C., and Sharp, M. J.: Measurement and parameterization of aerodynamic roughness length variations at Haut Glacier d'Arolla, Switzerland, Journal of Glaciology, 52, 281-297, 2006.

Brock, B. W., Willis, I. C., Sharp, M. J., and Arnold, N. S.: Modelling seasonal and spatial variations in the surface energy
860 balance of Haut Glacier d'Arolla, Switzerland, Annals of Glaciology, 31, 53-62, 2000.

Bukovsky, M. S. and Karoly, D. J.: A Brief Evaluation of Precipitation from the North American Regional Reanalysis, Journal of Hydrometeorology, 8, 837-846, 2007.

Carenzo, M., Pellicciotti, F., Rimkus, S., and Burlando, P.: Assessing the transferability and robustness of an enhanced temperature-index glacier-melt model, Journal of Glaciology, 55, 258-274, 2009.

865 Cazenave, A. and Cozannet, G. L.: Sea level rise and its coastal impacts, Earth's Future, 2, 15-34, 2014.

Chambers, J. R., Smith, M. W., Quincey, D. J., Carrivick, J. L., Ross, A. N., and James, M. R.: Glacial Aerodynamic Roughness Estimates: Uncertainty, Sensitivity, and Precision in Field Measurements, Journal of Geophysical Research: Earth Surface, 125, e2019JF005167, 2020.

Che, Y., Zhang, M., Li, Z., Wei, Y., Nan, Z., Li, H., Wang, S., and Su, B.: Energy balance model of mass balance and its
870 sensitivity to meteorological variability on Urumqi River Glacier No. 1 in the Chinese Tien Shan, Scientific reports, 9, 1-13, 2019.

Chen, J. and Brissette, F. P.: Hydrological modelling using proxies for gauged precipitation and temperature, Hydrological Processes, 31, 3881-3897, 2017.

Clarke, G. K., Jarosch, A. H., Anslow, F. S., Radić, V., and Menounos, B.: Projected deglaciation of western Canada in the
875 twenty-first century, Nature Geoscience, 2015. 2015.

Cofiño, A., Cano, R., Sordo, C., Primo, C., and Gutiérrez, J.: MeteoLab, a software library for Matlab>= 5 implementing statistical and data mining techniques for Meteorology, Applied Meteorology Group. Universidad de Cantabria, 2004. 2004.

Cogley, J. G.: Geodetic and direct mass-balance measurements: comparison and joint analysis, Annals of Glaciology, 50, 96-100, 2009.

880 Cogley, J. G. and Adams, W.: Mass balance of glaciers other than the ice sheets, Journal of Glaciology, 44, 315-325, 1998.

Comeau, L. E., Pietroniro, A., and Demuth, M. N.: Glacier contribution to the North and South Saskatchewan rivers, Hydrological Processes, 23, 2640-2653, 2009.

Cuffey, K. M. and Paterson, W. S. B.: The physics of glaciers, Butterworth-Heinemann/Elsevier, Burlington, Mass., 2010.

Dadic, R., Mott, R., Lehning, M., and Burlando, P.: Wind influence on snow depth distribution and accumulation over glaciers,
885 Journal of Geophysical Research: Earth Surface, 115, 2010.

Demuth, M.: Glaciers/Mountains as Monuments. In: 2018 State of the Mountains Report, Volume 1, Changing Glaciers, Changing Rivers, L, P., Z, R., and D, K. (Eds.), Alpine Club of Canada, 2018.

Demuth, M. and Horne, G.: Decadal-centenary glacier mass changes and their variability, Jasper National Park, Alberta, including the Columbia Icefield region. Geological Survey of Canada Open File 8229, 2018.

890 Demuth, M., Munro, D., and Young, G. (Eds.): Peyto Glacier: One Century of Science, National Hydrology Research Institute Science Report 8, Environment Canada, Natural Resources Canada and Alberta Environment, 2006.

Demuth, M. and Pietroniro, A.: The impact of climate change on the glaciers of the Canadian Rocky Mountain eastern slopes and implications for water resource adaptation in the Canadian prairies., 162 pp., 2002.

Demuth, M., Pinard, V., Pietroniro, A., Luckman, B., Hopkinson, C., Dornes, P., and Comeau, L.: Recent and past-century
895 variations in the glacier resources of the Canadian Rocky Mountains: Nelson River system, Terra Glacialis, 11, 27-52, 2008.

Déry, S. J., Stahl, K., Moore, R., Whitfield, P., Menounos, B., and Burford, J. E.: Detection of runoff timing changes in pluvial, nival, and glacial rivers of western Canada, Water Resources Research, 45, 2009.

Dittmer, K.: Changing streamflow on Columbia basin tribal lands—climate change and salmon, Climatic Change, 120, 627-641, 2013.

900   Ebrahimi, S. and Marshall, S. J.: Surface energy balance sensitivity to meteorological variability on Haig Glacier, Canadian
Rocky Mountains, The Cryosphere, 10, 2799-2819, 2016.

Ednie, M., Demuth, M., and Shepherd, B.: Mass balance of the Athabasca and Saskatchewan sectors of the Columbia Icefield,
Alberta for 2015 and 2016. Geological Survey of Canada, 2017.

Elsberg, D. H., Harrison, W. D., Echelmeyer, K. A., and Krimmel, R. M.: Quantifying the effects of climate and surface change
905   on glacier mass balance, Journal of Glaciology, 47, 649-658, 2001.

Engelhardt, M., Schuler, T. V., and Andreassen, L. M.: Sensitivities of glacier mass balance and runoff to climate perturbations
in Norway, Annals of Glaciology, 56, 79-88, 2015.

Erler, A. R., Peltier, W. R., and d'Orgeville, M.: Dynamically downscaled high-resolution hydroclimate projections for western
Canada, Journal of Climate, 28, 423-450, 2015.

910   Escanilla-Minchel, R., Alcayaga, H., Soto-Alvarez, M., Kinnard, C., and Urrutia, R.: Evaluation of the Impact of Climate
Change on Runoff Generation in an Andean Glacier Watershed, Water, 12, 3547, 2020.

Fiddes, J. and Gruber, S.: TopoSCALE v. 1.0: downscaling gridded climate data in complex terrain, Geoscientific Model
Development, 7, 387-405, 2014.

Fitzpatrick, N., Radić, V., and Menounos, B.: A multi-season investigation of glacier surface roughness lengths through in situ
915   and remote observation, The Cryosphere, 13, 1051-1071, 2019.

Fountain, A. G. and Tangborn, W. V.: The effect of glaciers on streamflow variations, Water Resources Research, 21, 579-
586, 1985.

Fujita, K.: Effect of precipitation seasonality on climatic sensitivity of glacier mass balance, Earth and Planetary Science
Letters, 276, 14-19, 2008.

920   Gabbi, J., Carenzo, M., Pellicciotti, F., Bauder, A., and Funk, M.: A comparison of empirical and physically based glacier
surface melt models for long-term simulations of glacier response, Journal of Glaciology, 60, 1140-1154, 2014.

Gerbaux, M., Genthon, C., Etchevers, P., Vincent, C., and Dedieu, J.: Surface mass balance of glaciers in the French Alps:
distributed modeling and sensitivity to climate change, Journal of Glaciology, 51, 561-572, 2005.

Giorgi, F.: Regional climate modeling: Status and perspectives, 2006, 101-118.

925   Grah, O. and Beaulieu, J.: The effect of climate change on glacier ablation and baseflow support in the Nooksack River basin
and implications on Pacific salmonid species protection and recovery, Climatic Change, 120, 657-670, 2013.

Harpold, A. A. and Brooks, P. D.: Humidity determines snowpack ablation under a warming climate, Proceedings of the
National Academy of Sciences, 115, 1215-1220, 2018.

Harrison, W., Cox, L., Hock, R., March, R., and Pettit, E.: Implications for the dynamic health of a glacier from comparison
930   of conventional and reference-surface balances, Annals of Glaciology, 50, 25-30, 2009.

Hersbach, H. and Dee, D.: ERA5 reanalysis is in production, ECMWF newsletter, 147, 5-6, 2016.

Hirose, J. and Marshall, S.: Glacier meltwater contributions and glaciometeorological regime of the Illecillewaet River Basin,
British Columbia, Canada, Atmosphere-ocean, 51, 416-435, 2013.

Hock, R.: A distributed temperature-index ice-and snowmelt model including potential direct solar radiation, Journal of
935   Glaciology, 45, 101-111, 1999.

Hock, R.: Glacier melt: a review of processes and their modelling, Progress in Physical Geography: Earth and Environment,
29, 362-391, 2005.

Hock, R.: Temperature index melt modelling in mountain areas, Journal of Hydrology, 282, 104-115, 2003.

Hock, R., Bliss, A., Marzeion, B., Giesen, R. H., Hirabayashi, Y., Huss, M., Radić, V., and Slangen, A. B.: GlacierMIP–A
940   model intercomparison of global-scale glacier mass-balance models and projections, Journal of Glaciology, 65, 453-467,
2019.

Hock, R. and Holmgren, B.: A distributed surface energy-balance model for complex topography and its application to
Storglaciären, Sweden, Journal of Glaciology, 51, 25-36, 2005.

Hock, R. and Holmgren, B.: Some aspects of energy balance and ablation of Storglaciären, northern Sweden, Geografiska
945   Annaler: Series A, Physical Geography, 78, 121-131, 1996.

Hock, R., Radić, V., and De Woul, M.: Climate sensitivity of Storglaciären, Sweden: an intercomparison of mass-balance
models using ERA-40 re-analysis and regional climate model data, Annals of Glaciology, 46, 342-348, 2007.

Hofer, M., Mölg, T., Marzeion, B., and Kaser, G.: Empirical-statistical downscaling of reanalysis data to high-resolution air temperature and specific humidity above a glacier surface (Cordillera Blanca, Peru), Journal of Geophysical Research: Atmospheres, 115, 2010.

Hunter, C., Moore, R. D., and McKendry, I.: Evaluation of the North American Regional Reanalysis (NARR) precipitation fields in a topographically complex domain, Hydrological Sciences Journal, 65, 786-799, 2020.

Huss, M., Bookhagen, B., Huggel, C., Jacobsen, D., Bradley, R. S., Clague, J. J., Vuille, M., Buytaert, W., Cayan, D. R., and Greenwood, G.: Toward mountains without permanent snow and ice, Earth's Future, 5, 418-435, 2017.

Huss, M. and Fischer, M.: Sensitivity of Very Small Glaciers in the Swiss Alps to Future Climate Change, Frontiers in Earth Science, 4, 2016.

Huss, M. and Hock, R.: Global-scale hydrological response to future glacier mass loss, Nature Climate Change, 8, 135-140, 2018.

Huss, M. and Hock, R.: A new model for global glacier change and sea-level rise, Frontiers in Earth Science, 3, 2015.

Huss, M., Hock, R., Bauder, A., and Funk, M.: Conventional versus reference-surface mass balance, Journal of Glaciology, 58, 278-286, 2012.

IPCC: Annex I: Atlas of Global and Regional Climate Projections, Cambridge University Press, Cambridge, United Kingdom and New York, NY, USA, 1311-1394 pp., 2013.

Jansson, P., Hock, R., and Schneider, T.: The concept of glacier storage: a review, Journal of Hydrology, 282, 116-129, 2003.

Jennings, K. S., Winchell, T. S., Livneh, B., and Molotch, N. P.: Spatial variation of the rain–snow temperature threshold across the Northern Hemisphere, Nature Communications, 9, 1148, 2018.

Johnson, E. and Rupper, S.: An Examination of Physical Processes That Trigger the Albedo-Feedback on Glacier Surfaces and Implications for Regional Glacier Mass Balance Across High Mountain Asia, Frontiers in Earth Science, 8, 2020.

Kistler, R., Kalnay, E., Collins, W., Saha, S., White, G., Woollen, J., Chelliah, M., Ebisuzaki, W., Kanamitsu, M., and Kousky, V.: The NCEP–NCAR 50-year reanalysis: monthly means CD-ROM and documentation, Bulletin of the American Meteorological society, 82, 247-268, 2001.

Klok, E. and Oerlemans, J.: Model study of the spatial distribution of the energy and mass balance of Morteratschgletscher, Switzerland, Journal of Glaciology, 48, 505-518, 2002.

Klok, E. and Oerlemans, J.: Modelled climate sensitivity of the mass balance of Morteratschgletscher and its dependence on albedo parameterization, International Journal of Climatology: A Journal of the Royal Meteorological Society, 24, 231-245, 2004.

Knap, W., Reijmer, C., and Oerlemans, J.: Narrowband to broadband conversion of Landsat TM glacier albedos, International Journal of Remote Sensing, 20, 2091-2110, 1999.

Konzelmann, T., van de Wal, R. S., Greuell, W., Bintanja, R., Henneken, E. A., and Abe-Ouchi, A.: Parameterization of global and longwave incoming radiation for the Greenland Ice Sheet, Global and Planetary change, 9, 143-164, 1994.

Lutz, S., Anesio, A. M., Jorge Villar, S. E., and Benning, L. G.: Variations of algal communities cause darkening of a Greenland glacier, FEMS Microbiology Ecology, 89, 402-414, 2014.

MacDonell, S., Kinnard, C., Mölg, T., Nicholson, L., and Abermann, J.: Meteorological drivers of ablation processes on a cold glacier in the semi-arid Andes of Chile, The Cryosphere, 7, 1513-1526, 2013.

MacDougall, A. H. and Flowers, G. E.: Spatial and Temporal Transferability of a Distributed Energy-Balance Glacier Melt Model, Journal of Climate, 24, 1480-1498, 2011.

Marshall, S. J. and Miller, K.: Seasonal and interannual variability of melt-season albedo at Haig Glacier, Canadian Rocky Mountains, The Cryosphere, 14, 3249-3267, 2020.

Marshall, S. J., White, E. C., Demuth, M. N., Bolch, T., Wheate, R., Menounos, B., Beedle, M. J., and Shea, J. M.: Glacier water resources on the eastern slopes of the Canadian Rocky Mountains, Canadian Water Resources Journal, 36, 109-134, 2011.

Marzeion, B., Jarosch, A. H., and Hofer, M.: Past and future sea-level change from the surface mass balance of glaciers, The Cryosphere, 6, 1295-1322, 2012.

Menounos, B., Hugonnet, R., Shean, D., Gardner, A., Howat, I., Berthier, E., Pelto, B., Tennant, C., Shea, J., and Noh, M. J.: Heterogeneous changes in western North American glaciers linked to decadal variability in zonal wind strength, Geophysical Research Letters, 46, 200-209, 2019.

Mesinger, F., DiMego, G., Kalnay, E., Mitchell, K., Shafran, P. C., Ebisuzaki, W., Jović, D., Woollen, J., Rogers, E., and Berbery, E. H.: North American regional reanalysis, Bulletin of the American Meteorological Society, 87, 343-360, 2006.

Milner, A. M., Khamis, K., Battin, T. J., Brittain, J. E., Barrand, N. E., Füreder, L., Cauvy-Fraunié, S., Gíslason, G. M., Jacobsen, D., and Hannah, D. M.: Glacier shrinkage driving global changes in downstream systems, Proceedings of the National Academy of Sciences, 114, 9770-9778, 2017.

Mölg, T., Cullen, N. J., Hardy, D. R., Kaser, G., and Klok, L.: Mass balance of a slope glacier on Kilimanjaro and its sensitivity to climate, International Journal of Climatology: A Journal of the Royal Meteorological Society, 28, 881-892, 2008.

Mölg, T., Großhauser, M., Hemp, A., Hofer, M., and Marzeion, B.: Limited forcing of glacier loss through land-cover change on Kilimanjaro, Nature Climate Change, 2, 254, 2012.

Mölg, T. and Kaser, G.: A new approach to resolving climate-cryosphere relations: Downscaling climate dynamics to glacier-scale mass and energy balance without statistical scale linking, Journal of Geophysical Research: Atmospheres, 116, 2011.

Moore, R., Fleming, S., Menounos, B., Wheate, R., Fountain, A., Stahl, K., Holm, K., and Jakob, M.: Glacier change in western North America: influences on hydrology, geomorphic hazards and water quality, Hydrological Processes: An International Journal, 23, 42-61, 2009.

Munro, D. S.: Surface roughness and bulk heat transfer on a glacier: comparison with eddy correlation, Journal of Glaciology, 35, 343-348, 1989.

Nash, J. E. and Sutcliffe, J. V.: River flow forecasting through conceptual models part I—A discussion of principles, Journal of hydrology, 10, 282-290, 1970.

Oerlemans, J.: Glaciers and climate change, CRC Press, 2001.

Oerlemans, J., Anderson, B., Hubbard, A., Huybrechts, P., Johannesson, T., Knap, W., Schmeits, M., Stroeven, A., Van de Wal, R., and Wallinga, J.: Modelling the response of glaciers to climate warming, Climate dynamics, 14, 267-274, 1998.

Oerlemans, J., Giesen, R., and Van den Broeke, M.: Retreating alpine glaciers: increased melt rates due to accumulation of dust (Vadret da Morteratsch, Switzerland), Journal of Glaciology, 55, 729-736, 2009.

Oerlemans, J. and Knap, W.: A 1 year record of global radiation and albedo in the ablation zone of Morteratschgletscher, Switzerland, Journal of Glaciology, 44, 231-238, 1998.

Oke, T.: Boundary layer climates, 0415043190, 1987.

Orsolini, Y., Wegmann, M., Dutra, E., Liu, B., Balsamo, G., Yang, K., de Rosnay, P., Zhu, C., Wang, W., Senan, R., and Arduini, G.: Evaluation of snow depth and snow cover over the Tibetan Plateau in global reanalyses using in situ and satellite remote sensing observations, The Cryosphere, 13, 2221-2239, 2019.

Østby, T. I., Schuler, T., Hagen, J. O. M., Hock, R., Kohler, J., and Reijmer, C.: Diagnosing the decline in climatic mass balance of glaciers in Svalbard over 1957-2014, The Cryosphere, 11, 191-215, 2017.

Petersen, L. and Pellicciotti, F.: Spatial and temporal variability of air temperature on a melting glacier: Atmospheric controls, extrapolation methods and their effect on melt modeling, Juncal Norte Glacier, Chile, Journal of Geophysical Research: Atmospheres, 116, 2011.

Petts, G., Gurnell, A., and Milner, A.: Eco-hydrology: new opportunities for research on glacier-fed rivers, Peyto Glacier: One Century of Science, 8, 255-275, 2006.

Prudhomme, C., Wilby, R. L., Crooks, S., Kay, A. L., and Reynard, N. S.: Scenario-neutral approach to climate change impact studies: application to flood risk, Journal of Hydrology, 390, 198-209, 2010.

Radić, V., Bliss, A., Beedlow, A. C., Hock, R., Miles, E., and Cogley, J. G.: Regional and global projections of twenty-first century glacier mass changes in response to climate scenarios from global climate models, Climate Dynamics, 42, 37-58, 2014.

Radić, V. and Hock, R.: Modeling future glacier mass balance and volume changes using ERA-40 reanalysis and climate models: A sensitivity study at Storglaciären, Sweden, Journal of Geophysical Research: Earth Surface, 111, 2006.

Radic, V., Tessema, M., Menounos, B., and Fitzpatrick, N.: Evaluation of Dynamically Downscaled Near-surface Mass and Energy Fluxes for Three Mountain Glaciers, British Columbia, Canada, 2018.

Rea, B. R.: Defining modern day Area-Altitude Balance Ratios (AABRs) and their use in glacier-climate reconstructions, Quaternary Science Reviews, 28, 237-248, 2009.

Réveillet, M., Six, D., Vincent, C., Rabatel, A., Dumont, M., Lafaysse, M., Morin, S., Vionnet, V., and Litt, M.: Relative performance of empirical and physical models in assessing the seasonal and annual glacier surface mass balance of Saint-Sorlin Glacier (French Alps), The Cryosphere, 12, 1367-1386, 2018.

Réveillet, M., Vincent, C., Six, D., and Rabatel, A.: Which empirical model is best suited to simulate glacier mass balances?, Journal of Glaciology, 63, 39-54, 2017.

Rye, C. J., Arnold, N. S., Willis, I. C., and Kohler, J.: Modeling the surface mass balance of a high Arctic glacier using the ERA-40 reanalysis, Journal of Geophysical Research: Earth Surface, 115, 2010.

Sandford, R. W.: The Columbia Icefield–3rd Edition, Rocky Mountain Books Ltd, 2016.

Schindler, D. W. and Donahue, W. F.: An impending water crisis in Canada's western prairie provinces, Proceedings of the National Academy of Sciences, 103, 7210-7216, 2006.

Shannon, S., Smith, R., Wiltshire, A., Payne, T., Huss, M., Betts, R., Caesar, J., Koutroulis, A., Jones, D., and Harrison, S.: Global glacier volume projections under high-end climate change scenarios, The Cryosphere, 13, 325-350, 2019.

Shean, D. E., Alexandrov, O., Moratto, Z. M., Smith, B. E., Joughin, I. R., Porter, C., and Morin, P.: An automated, open-source pipeline for mass production of digital elevation models (DEMs) from very-high-resolution commercial stereo satellite imagery, ISPRS Journal of Photogrammetry and Remote Sensing, 116, 101-117, 2016.

Smith, T., Smith, M. W., Chambers, J. R., Sailer, R., Nicholson, L., Mertes, J., Quincey, D. J., Carrivick, J. L., and Stiperski, I.: A scale-dependent model to represent changing aerodynamic roughness of ablating glacier ice based on repeat topographic surveys, Journal of Glaciology, 66, 950-964, 2020.

Takeuchi, N., Kohshima, S., and Seko, K.: Structure, formation, and darkening process of albedo-reducing material (cryoconite) on a Himalayan glacier: a granular algal mat growing on the glacier, Arctic, Antarctic, and Alpine Research, 33, 115-122, 2001.

Tennant, C. and Menounos, B.: Glacier change of the Columbia Icefield, Canadian Rocky Mountains, 1919–2009, Journal of Glaciology, 59, 671-686, 2013.

Tennant, C., Menounos, B., Wheate, R., and Clague, J.: Area change of glaciers in the Canadian Rocky Mountains, 1919 to 2006, The Cryosphere, 6, 1541-1552, 2012.

Teutschbein, C. and Seibert, J.: Bias correction of regional climate model simulations for hydrological climate-change impact studies: Review and evaluation of different methods, Journal of Hydrology, 456-457, 12-29, 2012.

Thibert, E., Blanc, R., Vincent, C., and Eckert, N.: Glaciological and volumetric mass-balance measurements: error analysis over 51 years for Glacier de Sarennes, French Alps, Journal of Glaciology, 54, 522-532, 2008.

Trouet, V. and Van Oldenborgh, G. J.: KNMI Climate Explorer: a web-based research tool for high-resolution paleoclimatology, Tree-Ring Research, 69, 3-13, 2013.

Trubilowicz, J. W., Shea, J. M., Jost, G., and Moore, R. D.: Suitability of North American Regional Reanalysis (NARR) output for hydrologic modelling and analysis in mountainous terrain, Hydrological Processes, 30, 2332-2347, 2016.

Vionnet, V., Marsh, C. B., Menounos, B., Gascoin, S., Wayand, N. E., Shea, J., Mukherjee, K., and Pomeroy, J. W.: Multi-scale snowdrift-permitting modelling of mountain snowpack, The Cryosphere, 15, 743-769, 2021.

Wagenbrenner, N. S., Forthofer, J. M., Lamb, B. K., Shannon, K. S., and Butler, B. W.: Downscaling surface wind predictions from numerical weather prediction models in complex terrain with WindNinja, Atmos. Chem. Phys., 16, 5229-5241, 2016.

Wetterhall, F., Pappenberger, F., He, Y., Freer, J., and Cloke, H. L.: Conditioning model output statistics of regional climate model precipitation on circulation patterns, Nonlin. Processes Geophys., 19, 623-633, 2012.

Wheler, B. A.: Glacier melt modelling in the Donjek Range, St. Elias Mountains, Yukon Territory, 2009. Dept. of Earth Sciences-Simon Fraser University, 2009.

Zemp, M., Huss, M., Thibert, E., Eckert, N., McNabb, R., Huber, J., Barandun, M., Machguth, H., Nussbaumer, S. U., Gärtner-Roer, I., Thomson, L., Paul, F., Maussion, F., Kutuzov, S., and Cogley, J. G.: Global glacier mass changes and their contributions to sea-level rise from 1961 to 2016, Nature, 568, 382-386, 2019.

Zemp, M., Thibert, E., Huss, M., Stumm, D., Denby, C. R., Nuth, C., Nussbaumer, S., Moholdt, G., Mercer, A., and Mayer, C.: Uncertainties and re-analysis of glacier mass balance measurements, The Cryosphere Discussions, 7, 789-839, 2013.